Volumetric Printing of Arbitrary Geometries via Tomographic Back-projection

Callum Vidler

Supervisor: Dr Mathew Joosten

School of Engineering
Deakin University

This dissertation is submitted for the degree of
Bachelor of Mechanical Engineering

February 2020

Declaration

I hereby declare that except where specific reference is made to the work of others, the contents of this dissertation are original and have not been submitted in whole or in part for consideration for any other degree or qualification in this, or any other university. This dissertation is my own work and contains nothing which is the outcome of work done in collaboration with others, except as specified in the text and Acknowledgements.

Callum Vidler
February 2020

Acknowledgements

I would like to thank the Deakin Digital Design and Engineering Centre (3DEC) and Deakin School of Engineering for the financial support to get this project up and running. Without their generous contribution this project would not have been able to advance. I would like to Dr. Mathew Joosten for the ongoing support and assistance through the project, his key insight was invaluable to the project. Futhermore, I would like to thank Dr. Rachel Rossau, Dr. Reza Parvizi and Mr. Tim Clark for their continuing technical support for the project and assistance with equipment and chemical ordering. Finally, I would like to thank my partner Dr. Anna Withanage for here immense emotional support.

Abstract

The advent of additive manufacturing has enabled professionals and hobbyists alike the ability to rapidly produce complex typologies with the geometric freedom like never before. However, despite the enormous benefits of additive manufacturing, the layer-by-layer deposition of material tends to result in significant sacrifices in terms of speed, geometric freedom and surface quality. This work demonstrates a significant paradigm shift in the area of additive manufacturing by enabling the whole print volume to be generated simultaneously in-situ, via sequential targeted illumination of a rotating resin volume. In this work we have demonstrated the development of a new slicing algorithm for volumetric printing that is capable of taking any arbitrary geometry and representing it as a set of integral projections. Furthermore, this work established a new acrylate polymer resin that is capable of supporting printed geometries without the need of complex supporting networks, in addition to two prototype mechanical devices that are capable of producing highly collimated pattern targeted illumination. The developed process enables construction of components in the order of 30 - 120 s for a set of diverse centimeter scale geometries.

Table of contents

List of figures **xi**

List of tables **xv**

1 Introduction **1**
1.1 Project Aim and Deliverables 3
1.2 Stakeholder Requirements 3
1.3 Project Benefits and Implications 3

2 Literature Review **7**
2.1 Printing systems 7
2.2 Photoinduced polymerization systems 13
2.3 Photo-polymerization Kinetics 16
2.4 Computed Tomography 18

3 Methodology **23**
3.1 Projection Algorithm 23
3.2 Resin Kinetics Model 28
3.3 Biaxial Thresholding 31
3.4 Reconstruction Algorithm Flowchart 33
3.5 3D Reconstruction 34
3.6 Mechanical Design 36
3.6.1 Volume MK1 36
3.6.2 Volume MK2 37
3.7 Resin Development 39
3.8 Resin Fabrication Methodology 41
3.9 Regeneration of Resin 42
3.10 Part Post-processing 42
3.11 Volumetric Exposure Time 43

3.12 Beam Divergence 44
3.13 Spin Up to Steady State 46
3.14 Overprinting Algorithm 47
3.15 Print Time Comparison 48
3.16 2D Calibration 48
3.17 3D Calibration 49
3.18 Mechanical Testing 50

4 Results **51**
4.1 Effect of Projection Angles 51
4.2 Tomographic Image Production 53
4.3 Tomographic Reconstruction 55
4.4 3D Curing Engine 58
4.5 Volumetric Slicer 60
4.6 Mechanical Design 61
4.6.1 Mechanical Design: Version 1 61
4.6.2 Mechanical Design: Version 2 62
4.7 Resin Development 64
4.8 Two-dimensional Calibration 66
4.9 Three-dimensional Calibration 67
4.10 Printing of a Sphere 68
4.11 Printing of a Cylinder 69
4.12 Printing of a Martini Glass 70
4.13 Volumetric Overprinting 71
4.14 Printing of a Simple Lens 72
4.15 Comparison of Print Times 73
4.16 Mechanical Characterization 74

5 Discussion/Future Work **77**

6 Conclusions **83**

References **85**

List of figures

2.1 Schematic of CLIP and CLIP like systems 8
2.2 Schematic of FDM system 9
2.3 Volumetric printing via holographic imaging 10
2.4 Operation of the CAL system 11
2.5 CAL system extended to elastomers 12
2.6 Volumetric printing of hydro-gels 12
2.7 Type I photoinitiation system 13
2.8 Type II photoinitiation system 14
2.9 Camphorquinone visible light absorption 15
2.10 Effect of concentrated oxygen on the light absorbance of common photo-initiators 17
2.11 First computed tomography images 18
2.12 Modern computed tomography 19
2.13 Iterative filtered back projection 20
2.14 Neural network architecture for computed tomography 20
2.15 Neural network limited angle tomography 21

3.1 Mesh to part cross-section 24
3.2 The radon transform 25
3.3 Effect of filtering on projection outcome 26
3.4 Projection algorithm 27
3.5 Kinetics model 29
3.6 Degree of cure graph 30
3.7 Rotational intensity variation of boundary points within the volume. . 31
3.8 Effect of transverse scaling on the output of the yoda target geometry. . 32
3.9 Illustration of how the target geometry point cloud is reconstructed from a series of projection images. 34

3.10 Evolution of the jaccard index for various projection angles of the Gyroid geometry. . . . 35
3.11 Volume MK1 Layout . . . 36
3.12 Volume MK2 Optical Layout . . . 38
3.13 Model sedimentation . . . 39
3.14 Volumetric print time . . . 44
3.15 Derivation of beam divergence . . . 45
3.16 Shadow occlusion algorithm . . . 47
3.17 Two-dimension curing calibration . . . 48
3.18 Three-dimension curing calibration . . . 49

4.1 Influence of projection angles . . . 51
4.2 Error with projection angles . . . 52
4.3 Effect of angle frequency on CPU time . . . 52
4.4 Volumetric algorithm output . . . 53
4.5 Volumetric algorithm output . . . 54
4.6 3D reconstruction of Yoda . . . 55
4.7 3D reconstruction of Yoda . . . 56
4.8 3D convergence plot . . . 57
4.9 Simulation of the eiffel tower geometry . . . 58
4.10 Simulation of the yoda geometry . . . 59
4.11 Components of the volumetric slicer . . . 60
4.12 Mechanical Design: Version 1 . . . 61
4.13 Mechanical Design: Version 2 . . . 62
4.14 Mechanical Design: Version 2 . . . 62
4.15 Mechanical Design: Version 2 . . . 63
4.16 Result of ultraviolet–visible spectroscopy on photo-initiator Igracure 819. 64
4.17 UV-VIS CQ+EDAB . . . 65
4.18 UV-VIS Comparison . . . 65
4.19 Developed resin . . . 65
4.20 Degree of cure map for two-dimensional printing . . . 66
4.21 Complex 2D projections . . . 66
4.22 Three-dimensional calibration of printing system . . . 67
4.23 Normalized time to cure for varying intensity functions . . . 68
4.24 Volumetric printing of a spherical geometry. . . . 68
4.25 Volumetric printing of cylindrical geometry. . . . 69
4.26 Volumetric printing of martini glass. . . . 70

4.27 Volumetric overprinting 71
4.28 Rapid manufacture of a simple cylindrical lens. 72
4.29 Comparison of print times for common additive manufacturing methods. 73
4.30 Mechanical strength of cast photo-polymer resin. 74
4.31 Volumetric printing of dog-bone 74
4.32 Mechanical testing of printed dog-bone 75

5.1 Transverse volumetric masking tomography 79
5.2 Point scanning volumetric tomography 80
5.3 Stationary vessel volumetric printing 81

List of tables

4.1 Print time comparison 73

Chapter 1

Introduction

Additive manufacturing has revolutionized the manufacturing industry since its first debut in the 1980's with the technique of stereo-lithography. Since then there has been significant manufacturing paradigm shift. This has resulted in products and geometries that once were unobtainable by traditional methods, becoming progressively more common. Today, additive manufacturing (AM) has grown significantly from its humble beginnings in the 1980's, with a plethora of AM technologies being currently available. Over the past 30 years various additive manufacturing technologies have been developed which can be separated into three distinct categories, depending on their unit operation (zero-dimensional, one-dimensional and two-dimensional).

As the majority of the AM methods today rely either on a zero-dimensional (0D) or a one-dimensional (1D) approach to three-dimensional (3D) printing. Zero-dimensional printing operations are those in which material is deposited at a single point for every time increment. Operations like these can be found in methods such as selective laser sintering (SLS), selective laser melting (SLM) and stereolithography (SLA). The abovementioned methods use a laser to fuse or cure material at discrete points. One-dimensional systems are also commonly used, most notably in fused deposition modeling (FDM), where material is extruded in small distinct portions to recreate the required geometry. More recently faster systems such as Digital Light Projection systems (DLP) or Continuous Liquid Interface Production (CLIP), use a 2D approach to 3D printing, in which single layers of the target volume are cured simultaneously by a light source, resulting in a significant decrease in print time, compared to their 1D and 0D counterparts. In all of these cases models are produced by serially stacking layer upon layer to produce the final 3D model.

Volumetric additive manufacturing is the latest technique developed that is capable of producing entire 3D objects in a single step via holography. This method leverages the effects of intensity superposition of three perpendicular beams consequently introducing a new 3D printing paradigm while demonstrating some significant advantages over traditional processes. However, this approach left a lot to be desired and could only be used to geometries with intercepting orthogonal images. The proposed method unlike the holography approach hopes to solve this problem by developing an approach that enables parts to be generated volumetrically, whilst maintaining the geometric flexibility present in other AM processes.

The proposed process unlike traditional methods does not generate geometry via a layer-by-layer approach, instead exposes a transparent resin at intermittent angles about its rotation axis, where the cumulative dose of these projections represent the target geometry. This approach demonstrates the fundamental advantage of volumetric 3D printing over a traditional layer by layer system, not only due to the reduction in the print time, but in the more robust and predictable mechanical properties. As the proposed approach alleviates the use of layers, the inherent weakness of AM, parts under this process behave isotropically, improving the predictability and properties of AM products. Furthermore, volumetric 3D printing enables geometries that are not available in traditional AM processes such as steep overhangs, to be produced without complex and wasteful support material. Therefore, the purpose of this project is to develop a capable volumetric 3D printing system and explore its innate benefits to the field of additive manufacturing.

1.1 Project Aim and Deliverables

This project aims to develop a robust algorithm that is capable of accurately representing any arbitrary geometry via a set of resin optimized tomographic back projections. Furthermore, the project aims to fabricate a volumetric 3D printing system that is capable of validating the aforementioned algorithm. The purpose of this project is to demonstrate the advantages of such system in comparison to traditional AM processes.

The completion of this project will deliver a robust system that is capable of converting any arbitrary geometry into a set of representative projections. Furthermore, the project will deliver a software package that encompasses the developed algorithm, enabling the technology to be easily used and accessed. Finally, the project will deliver a robust mechanical and optical characterization of the resin system, to aid in the continual development of this technology.

1.2 Stakeholder Requirements

As this project is not in collaboration with any external entities, the only involved stakeholders are Dr. Mathew Joosten and Deakin School of Engineering. The ideal requirements for this project from the point of view of these contributors is for the satisfactory completion of SEJ441 and SEJ446. However, from a research standpoint, the requirement of this project is to build a robust volumetric printing platform that is capable of producing any geometry via tomographic back projections. Hopefully, the completion of this project will spark interest into this new and emerging field and provide a strong base of knowledge from which additional innovation can grow.

1.3 Project Benefits and Implications

Unlike traditional additive manufacturing processes, the volumetric approach proposed in this project has significant benefits and implications, primarily in regards to print speed and mechanical properties. Currently available printing processes operate by sequentially stacking cross-sections of the target geometry. This approach in all cases is extremely slow as the target geometry has to either be traced out by the printer such as in FDM, or single incremental slices need to be exposed individually such as in CLIP.

Volumetric 3D printing solves this issue by allowing discrete volumes of a photosensitive resin to be cured simultaneously, greatly reducing the required print time. In theory, this approach could cure a unit volume in a single shot, by illuminating all possible angles simultaneously via a series of projectors. Such an approach would enable even faster print times that what is currently proposed, however for this project we have chosen a slightly slower approach, which uses a single projector with a rotating stage for a proof of concept.

Excluding the print duration benefits of the volumetric approach, another significant benefit of this technology is the reduction and possible illumination of print layers. discrete layers are an innate artifact of traditional AM systems due to their layer-by-layer approach. In contrast the volumetric printing method illuminates the target volume at various incremental angles around its azimuth, causing the model to be produced by the simultaneous voxilization of the resin, as each unit voxel overcomes the gel point. Because of this there are two primary benefits to this approach. First it is expected that the relative surface roughness will be significantly lower in comparison to a layer-by-layer approach, reducing the inherent stress concentrations at the layer interfaces and the ability for parts to be used for optical systems. Secondly, as traditional AM parts tend to be anisotropic due to the layer interactions, they are unpredictable and inconsistent. In contrast parts produced by a volumetric approach should exhibit isotropic behavior increasing the predictability and consistency of 3D printed parts.

The ability to produce parts with internal components has been a significant sought after application of 3D printing, as it would decrease the time required to produce assemblies. Examples of components have been produced by traditional AM processes, however they often are tedious and require prints to be paused at specific layer locations for manual insertion of componentry. A volumetric AM process will enable encloses to be manufactured around the component reducing the necessary assembly step and increasing part cycle time.

Chapter 2

Literature Review

2.1 Printing systems

The advent of additive manufacturing has caused a significant paradigm shift to the way in which products are made, resulting in amateurs and professionals alike to have the ability to produce useful products for everyday applications. Three-dimensional printing systems have evolved significantly since the application of sterolithography in the mid 1980's [1]. Though this is a relatively old technique, many of the printing systems currently available today still rely on the same or similar technology, as it provides a simple yet highly accurate method of producing 3D objects.

Sterolithography (SLA or SL) similar to its parent process lithography [2], produces objects sequentially layer-by-layer by selectively exposing regions of the objects cross-section to light [3]. Traditionally the approach taken by this method uses a photopolymerizable resin and a patterned illumination source to cure cross sections of the target geometry. The speed of many layer-by-layer SLA methods are dictated by the necessity of the printed model to be sequentially removed from the glass projection surface after each layer. This process in conjunction with resin settling and re-coating steps, often lead to print times that are unfavorable. Recent continuous liquid interface production (CLIP) [4] (Figure 2.1a) techniques hope to address this deficiency by using an oxygen-permeable window in place of a traditional projection window. The addition of an oxygen layer at the projection interface enables a polymerization-free resin layer, enabling continuous production by negating the need for part separation from the projection surface.

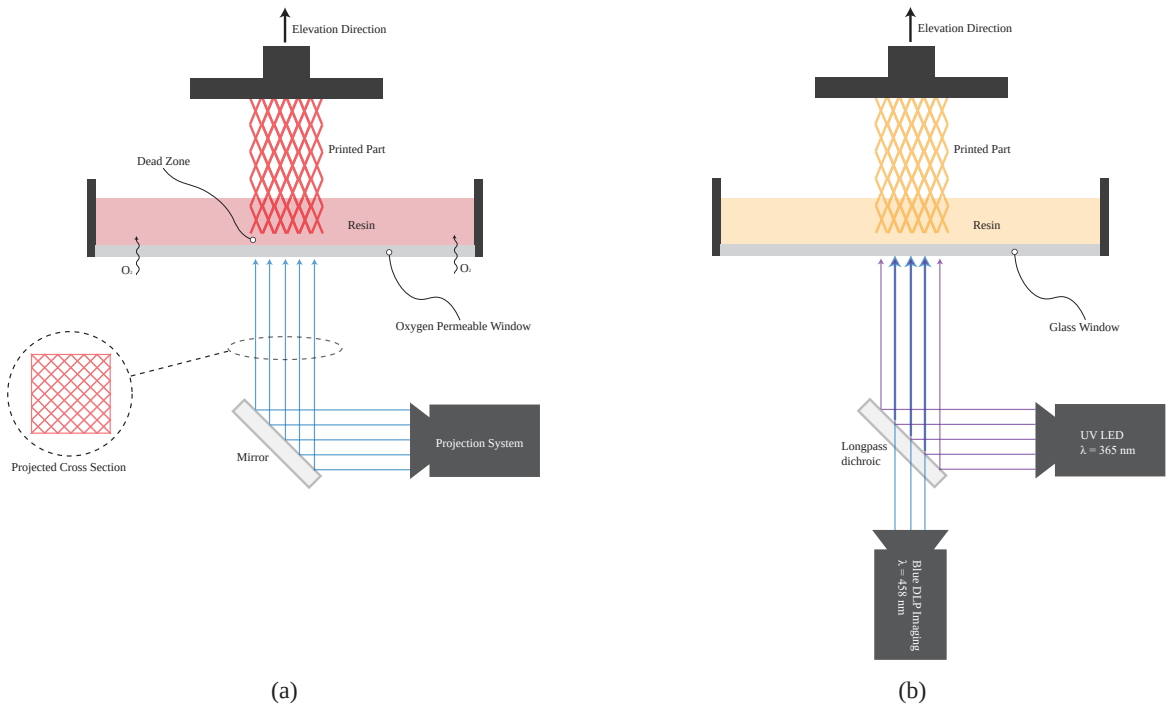

Fig. 2.1 (a) Schematic of a CLIP 3D printer, where continuous part production can be achieved by oxygen inhibition at the projection interface. (b) Schematic for rapid continuous printing via polymerization inhibition patterning.

More recently technology has been developed that enables a system to print continuously at high elevation velocities with the ability to expose layers in a single shot, without the need of an oxygen permeable window (Figure 2.1b) [5]. This process coined polymerization inhibition patterning, uses two illumination sources of different wavelengths to simultaneously inhibit and exhibit regions of the target cross-section. Patterned illumination from below the transparent dichroic lens initiates the polymerization of the resin, whereas illumination via the second projection source inhibits the reaction. This process enables the parts to be fabricated not only without the need of an oxygen permeable window, but a significantly quicker elevation velocities in comparison to the aforementioned CLIP technology [5].

More recently with the arrival of at home 3D printing [6], a more cost effective approach to 3D printing has emerged known as fused deposition modeling (FDM) (Figure 2.2). This approach similar to the aforementioned technologies, builds three dimensional structures by serially tracing out cross sections of the target geometry layer upon layer [7]. Unlike the above-mentioned stereo-lithography process which relies on the interaction of a photo curable resin with a light source , FDM primarily relies on the deposition of a molten polymer along a described path.

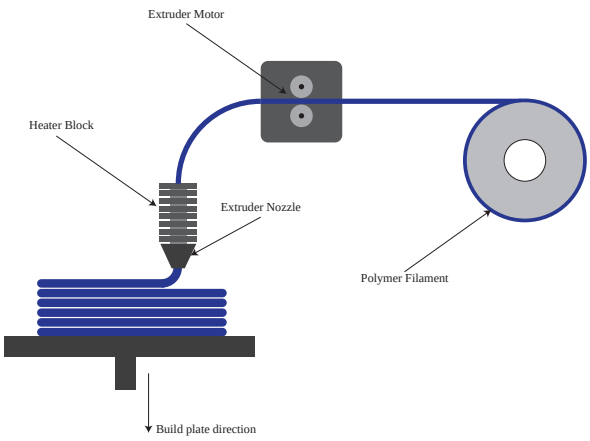

Fig. 2.2 Schematic for a fused deposition modeling system which highlights the technologies ability to produce parts by the sequential stacking of discrete slices.

The technologies listed above can be categorized by their unit operation, that is the operation taken by the printing system for each discrete time increment. Stereo-lithography based systems can be treated as a zero-dimensional approach to additive manufacturing [8], as single points are cured or deposited by each time unit operation. Similar approaches can also been seen in selective laser sintering (SLS) [9] and selective laser melting (SLM) [10], in which a powder matrix is selectively solidified. One-dimensional approaches such as fused deposition modeling generate geometry via physically 'tracing' the part out layer-by-layer. More recently 2D dimensional systems have been produced that enable complex fabrication via the simultaneous polymerization of two-dimensional slices of the model [11]. This approach enables a significantly faster method of production compared to its one-dimensional and zero-dimensional counterparts, however still leaves much to be desired.

Recent systems have been developed to produce parts via a three-dimensional approach, leading to a significant decrease in the required print duration. One of these systems coined holographic lithography [12] operates via using a diffractive element

to phase modulate a coherent laser array of sub images (Figure 2.3c). These images are positioned such that the superposition of each orthogonal image generates a target dose in the intensity of the required model (Figure 2.3a). The inherent benefit of this approach its the technologies ability to produce parts in situ, that is without the need of a complex support structure. Furthermore, due to this approaches ability to fabricate all regions in the target volume simultaneously (Figure 2.3b), traditional artifacts such as layer discontinuities are removed. However, though the advent of this approach pioneered a new era of volumetric additive manufacturing, the method could only be used for geometries which could be represented by the intersection of three orthogonal beams.

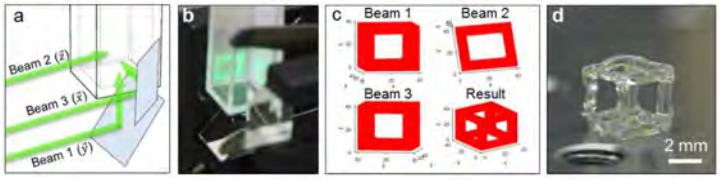

Fig. 2.3 (a) Representation of the incident beam geometry for the (b) Photo of the cuvette before filling with resin, with paper screens at two sides for visualization of the projected pattern (c) MATLAB point cloud representations of the propagating intensities for the three beams, and the region where they overlap in space. (d) The resulting part, after a single exposure of 12 s.[12]

Recent advances in the area of volumetric additive manufacturing have shown a significant step forward in the technologies ability to produce arbitrary geometries in a fraction of the time of conventional approaches. Computed Axial Lithography (CAL) [8] (Figure 2.4) is a new system that builds upon the concept highlighted by the holographic approach, however extends the gamut of available geometries. This process works by first generating a set of projections that accurately represent not only the target geometry but density information of the model [13]. These aperiodic projections are then back projected through a photo-curable polymer matrix at incremental angles around the volumes azimuth to reconstruct the model in situ. This method, similar to the holographic approach, operates by generating the models superposition within the resin volume, such that the cumulative light dose overcomes the localized gel-point of the sub-straight.

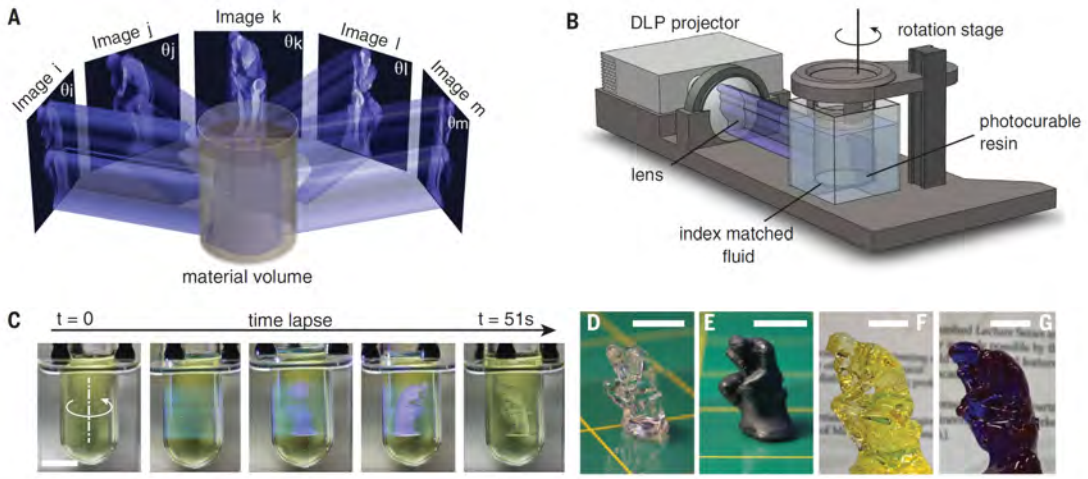

Fig. 2.4 (a)Underlying concept of patterned illumination required for the volumetric construction method (b) Generalized 3D printing setup (c) Sequential view of the build volume demonstrating how parts can be produced in situ (d-g) Examples of 3D printed geometries via computed axial lithography [8]

This approach unlike any other currently available systems, enables parts to be fabricated not only without the need of complex support structures, but with the absence of layer discontinuities. This is due to the fact that models are fabricated via the solidification of resin voxels and not via deposition or curing of layers. Therefore, parts produced via the CAL system unlike traditional AM technologies, exhibit isotropic behavior [14], allowing the potential for parts to be produced that are stronger and more predicable. Furthermore, as parts are produced in situ within the resin volume, CAL has the ability to produce geometry over or around already existing components, enabling the potential for complex assemblies of parts to be printed at once.

Recent applications of the CAL approach have been extended to other materials and lights sources [15], illustrating the ability for this approach to generate complex internal cavities for medical applications (Figure 2.5).

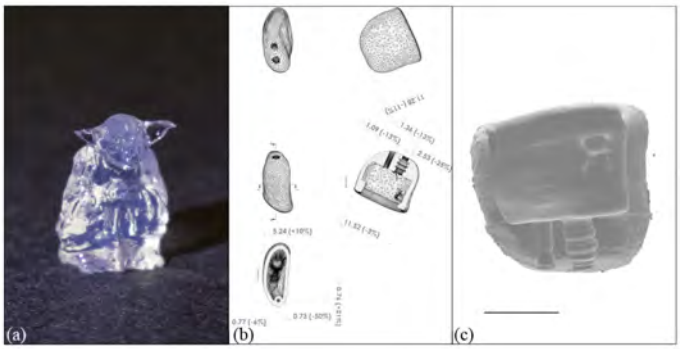

Fig. 2.5 (a)Yoda figure printed from elastomer material (b) MicroCT measurements of the printing accuracy with respect to the produced model (c) MicroCT representation of a printing hearing aid, highlighting the complex geometry within the volume [15]

Bio-fabrication technologies such as stereo-lithography and extrusion based techniques have revolutionized the medical industry enabling the fabrication of complex engineered tissues. However, this current technology relies on slow layer-by-layer processes that currently impart impaired cell functionality on 3D printed tissues. To overcome this challenge volumetric printing has been shown to be a viable option for producing cell-laden tissue constructs with high viability from gelatin-based photoresponsive hydrogels [16]. This technique has been shown to produce high fidelity working valves and cell impregnated meniscus-shaped structures (Figure 2.6).

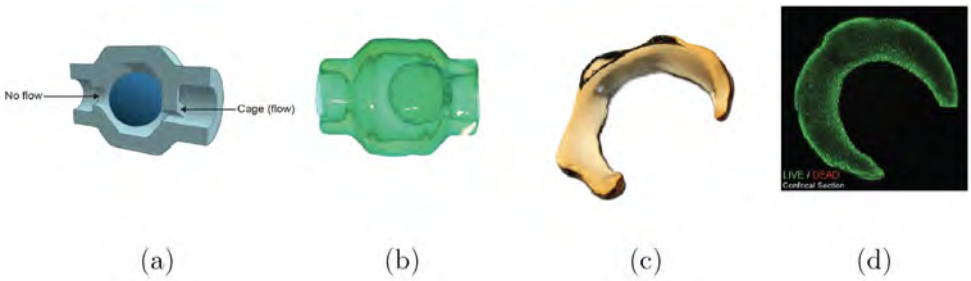

Fig. 2.6 **(a)** CAD representation of 3D printed valve structure **(b)** Top view of the volumetrically printed valve structure highlighting complex internal features. **(c)** 28 day in vitro cultured printed model of a representative meniscus. **(d)** high cell viability throughout the construct was observed over a 7 d period for the volumetrically printed model.

2.2 Photoinduced polymerization systems

Photoinduced polymerization systems is a rapidly expanding technology as it enables a rapid curing method that is primarily solvent free, energy efficient and generally economical [17]. Photo-polymerization systems have for the most time have been used for industrial applications such as printing, adhesives, composite materials and dental implants due to their high curing rate. More recently photoinduced polymerization has been used in stereo-lithography systems as it enables generation of high resolution polymer cross sections due to its ability to enable light based localized curing [18]. Acrylate based resin systems are most often used for light curable resin systems due to the high reactivity of the acrylate monomers. UV-irradiation in the presence of a suitable photo-initiator is one of the most efficient polymerization methods and is why UV curable systems are most frequently used in stereo-lithography applications such as SLA and CLIP.

Classification of photo-initiators are categorized by the mechanism in which polymerization occur, i.e. free radical, catonic or anionic [19] and have been developed over the years to obtain systems that exhibit faster curing rates, increased photo-sensitivity and polymer properties. These properties are often dictated by the type of photo-initiator used and thus the selection of this photo-initiator is critical in generating highly reactive resin formulations. Radical polymerization systems are the most widely used for 3D printing applications and are characterized by the nature of the mechanism that produces the free-radical intermediates upon irradiation of the initiators [20].

Type I photofragmentation systems (Figure 2.7) produce radical pairs via a highly efficient α-cleavage process. This class includes aromatic carbonyl compounds that undergo homolytic C-C bonds upon UV exposure. The primary benefit of type I system is its ability to produce radical pairs without the need of a secondary compounds, thus this process is usually more efficient than its type II counterpart [21].

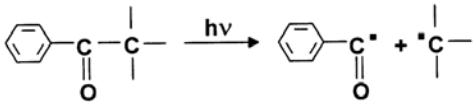

Fig. 2.7 Photofragmentation process present in type I radical polymerization systems

Type II systems (Figure 2.8) operate via hydrogen extraction from donor molecules and thus usually consist of two components, typically an aromatic ketone and a radical precursor containing a weak covalent bond.

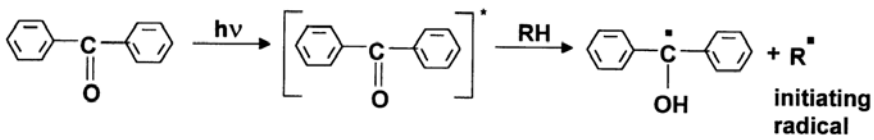

Fig. 2.8 Hydrogen extraction process present in type II radical polymerization systems

In most photopolymerization systems specifically type II systems, the inclusion of atmospheric oxygen has a significant determent to the quantum yields of initiating radicals. This generally leads to a significant retardation and inhibition of the polymerization process, as radical interaction with localized oxygen leads to inactive species. Therefore for most applications including stereo-lithography, it is often desirable to allow polymer formulations to be exposed to atmospheric conditions to equalize the oxygen concentration [22].

Camphorquinone (CQ) which is a blue light photo-initiator primarily used in dental applications, is one of the most common type II photo-initiators due to its high reactivity in the visible spectrum with a peak absorbtion of around $\lambda_{max} = 470nm$ [23]. As camphorquinone is a type II photo-initiator it is often paired with a strong co-initiation system such as ethyl 4-(dimethylamino)benzoate (EDAB) for hydrogen extraction. Aside from its use in dental applications CQ + EDAB systems have showed significant promise in the application of volumetric 3D printing, as they offer a robust curing system in the visible spectrum.

Camphorquinone has two primary absorption windows with the first being in the 200-300nm range via $\pi, \pi*$ transition and at 470nm (responsible for its yellow colour) due to the $n, \pi*$ transition of the dicarbonyl group (Figure 2.9) [24]. As with most photo-initiators camphorquinone is most frequently used with acrylate based resin systems and therefore enable a wide variety of material formulations to be used. As camphorquinone is a type II free-radical polymerization system the presence of oxygen results in a inbibition of the polymerization process via the oxidization to camphoric acid monoesters [25].

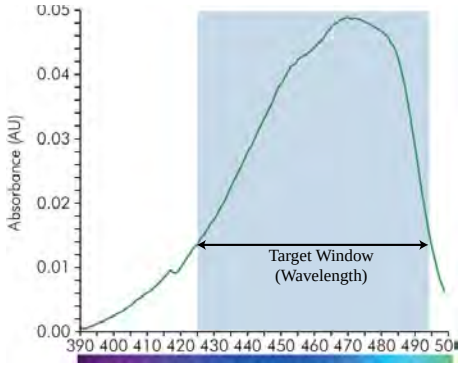

Fig. 2.9 Visible light absorption spectrum of camphorquinone, ranging from about 425 to 495 nm. [24]

The ability for volumetric 3D printing techniques to produce parts in situ, require resin formulations that exhibit extremely high viscosities. As acrylate resins begin the cure, the localized density of the resin begins to change resulting in a buoyant force present on the partially cured voxel [26]. In cases where the viscosity of the resin is low, these small changes in density cause the part to move during the duration of the print, and thus can normally be overcome with higher viscosity resins. High viscosity diacrylate based polymers such as poly(ethylene glycol) diacrylate (PEGDA) and bisphenol A glycerolate (1 glycerol/phenol) diacrylate (BPAGDA) have shown excellent promise in the use of volumetric 3D printing, not only for their ability to produce high viscosity resin systems, but for their compatibility with visible light photo-initiators such as camphorquinone [14].

2.3 Photo-polymerization Kinetics

With the increasing use of photo-polymerization systems in additive manufacturing [27] and dentistry [28] great work has gone into understanding the idiosyncrasies of these processes, both from a chemical and physical standpoint. These systems tend to be constructed from acrylate monomers coupled with a light-curable photo-initiator to achieve free-radical polymerization via the absorption of various wavelengths of light [25].

As these systems are becoming more prevalent for stereo-lithography applications [29], one frequently important characteristic is understanding the polymerization rate of these highly functional monomers. In general, the classical equation for polymerization rate is [30]:

$$R_{\mathrm{p}} = \frac{k_{\mathrm{p}}}{k_{\mathrm{t}}^{0.5}} [M] \left(R_{\mathrm{p}}/2\right)^{0.5} \tag{2.1}$$

Where [M] represents the concentration of the functional groups, R_i the initiation rate and k_p and k_t are the propagation and termination rate coefficients respectively. However, in the case of photo-chemical initiation process, such as what can be seen with three-dimensional printing resins, the polymerization rate takes the form of [31, 32].

$$R_{\mathrm{p}} = \frac{k_{\mathrm{p}}}{k_{\mathrm{t}}^{0.5}} [M] \left(\Phi I_{\mathrm{a}}\right)^{0.5} \tag{2.2}$$

Where Φ is the quantum yield for initiation and I_a is the absorbed intensity of light. Anseth *et al.* [33] was able to show that due to auto-acceleration at the initial stages of the reaction, k_t tends to decrease rapidly from the beginning of the polymerization reaction due to the onset of the gel effect. As the polymer approaches the maximum polymerization rate, the reaction becomes primarily diffusion controlled and thus a plateau is observed. In contrast, k_p remains relatively constant until higher conversion rates are reached and thus causing diffusion of the monomer to decrease [34].

The determination of such polymerization rates tends to be extremely complicated with respect to reaction kinetics, primarily due to early onset auto-acceleration and oxygen inhibition [35]. However, in general there tends to be two primary approaches to modeling photo-polymerization reactions. The model that is most widely used due

to its simplicity was developed by Tryson *et al.* [36] and is based on classical equations that assume that the only termination reaction is between two macro-radicals. Other fully integrated models described by Kabatc *et al.* [37] take a slightly more holistic approach by assuming the most probable, but albeit more complex solution. This approach assumes the usual bi-molecular interaction of polymer radicals, as well as a first order process involving only a single polymer radical, with both of these processes happening in parallel.

Thus, it can be shown that the polymerization rate for these quasi-parallel processes tend to be more accurately described as they do not assume rate linearization over time [38]. Thus, the equation for polymerization rate of mixed reactivity has been shown to be:

$$R_{\mathrm{p}}^{\mathrm{mix}} = \frac{k_{\mathrm{p}}}{4k_{\mathrm{t}}^{\mathrm{b}}}[M]\left\{\left[(k_{\mathrm{t}}^{\mathrm{m}})^2 + 16\phi k_{\mathrm{t}}^{\mathrm{b}}\right]^{0.5} - k_{\mathrm{t}}^{\mathrm{m}}\right\} \tag{2.3}$$

Recently, more complex models have been able to fully incorporate the effect of oxygen inhibition on the polymerization rate of the monomer, as concentrated oxygen first has to be depleted before cross-linking can occur [39] Fig.2.10. In general these models tend to be incomplete relying on significant assumptions about the state of the polymer and environmental conditions. Furthermore, changes in the viscosity of the oligomer during curing does not remain constant, which greatly impacts the diffusion of free-radicals that further limit the reactivity [40].

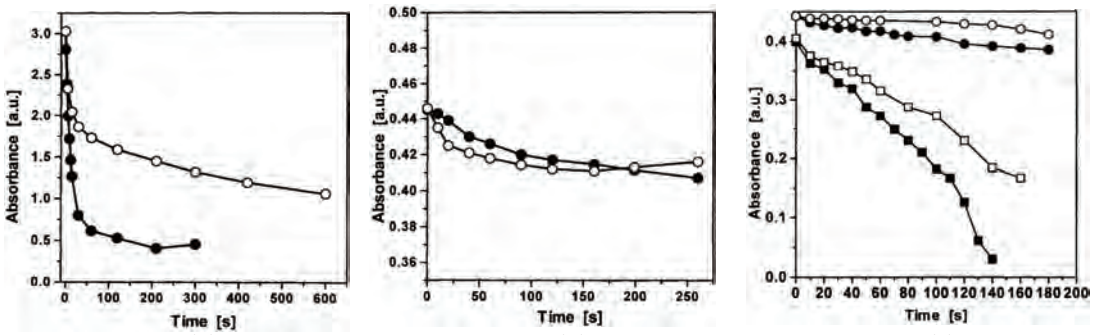

(a) (b) (c)

Fig. 2.10 Effect of concentrated oxygen on the light absorbance of common photo-initiators. (a) Depletion of EDAB in the 370nm range, (b) Depletion of CQ in the 470nm range with TEGDM, (c) Depletion of CQ in the 470nm range with TDM. Open markers represent nitrogen rich environment, whereas closed markers represent oxygen rich environment. [40]

2.4 Computed Tomography

An important problem in image processing is the ability to reconstruct a cross-sectional image from a set of the objects projections. This idea was first envisioned in the early 20th century by J. Radon, where he showed that certain two-dimensional manifolds could be described by the sum of their integral projections over straight lines [41].

$$(\mathcal{R}f)(s,\Theta) = \int_{x\in-\infty} f(x)dx = \int_{\Theta^{\perp}} f(s\Theta + y)dy \tag{2.4}$$

This concept remained somewhat abstract for a great number of years until A.M. Cormack was able to illustrate the possibility for this technique to be applied to radiological applications and served as the first initial basis of computed tomography [42]. It was shown that in a small set of topologies, it was possible to reconstruct a real function of finite planar region by the sum of the line integrals intersecting said region. With the aim of this approach to characterize the non-constant absorption coefficient for X-ray tomography, such that to achieve precise radiation dose in the region of interest.

It wasn't until G.N Hounsfield was able to adapt the approach taken by Cormack into a clinical sense with the first computerized transverse axial scanning tomography machine (CAT Scan) that the implications of such a technology became apparent [43]. Though rudimentary, this process was able to reconstruct an 80 × 80 numerical matrix, where the points represented the absorption coefficient of the corresponding volume of material in that slice Fig. 2.11.

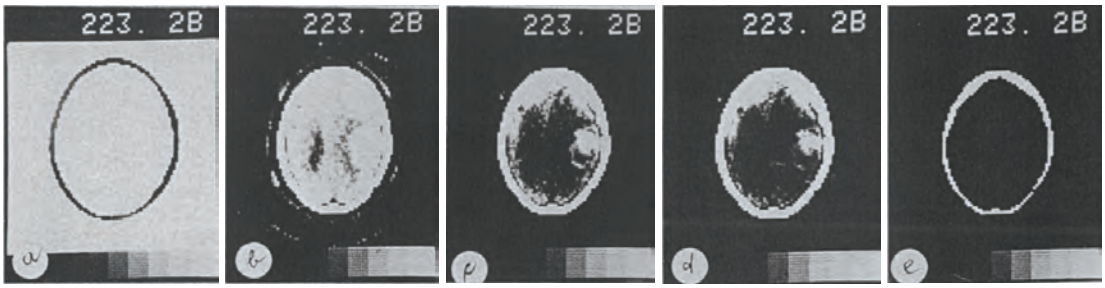

(a) (b) (c) (d) (e)

Fig. 2.11 First images produced by the computed tomography process, highlighting the ability for internal features to be identified by varying window level adjustment. (a) Represents patients hair, (b) Water in the ventricles, (c) Tumor and hemorrhage, (d) Hemorrhage details, (e) Skull bone.

The method outlined by Hounsfield worked by projecting and detecting attenuated X-rays from varying angles around the patient. These dose profiles could then be back-projected across the volume, revealing the volume(s) within. Nowdays imaging techniques using penetrating radiation usually leverage an array of detectors rather than just one, which enables a series of projections for each rotation of the scanner gantry Fig. 2.13 [44]. However, due to the number of detectors, noise if often present in the image due to beam hardening and high contrast edge effects, which can lead to image non-linearity causing artifacts such as streaking or cupping [45, 46].

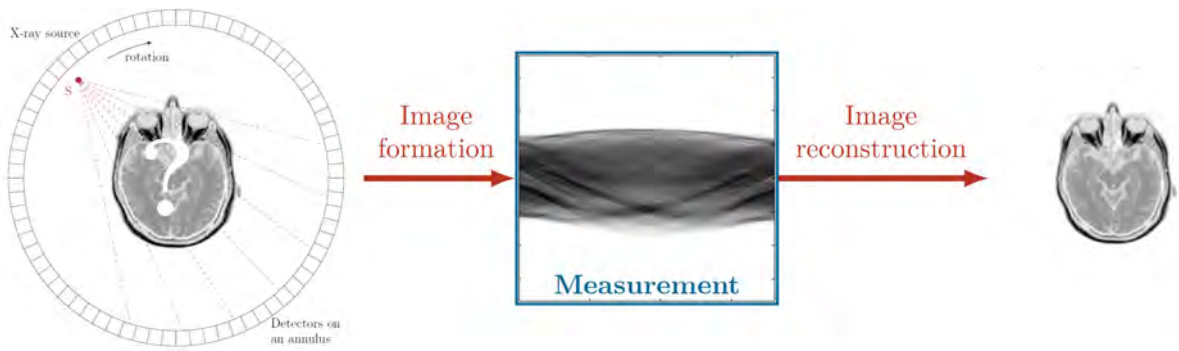

Fig. 2.12 Modern approach to computed tomography reconstruction. [44]

In an idealized scenario standard Fourier filtered back-projection algorithms can provide exact solutions to the inverse problem, however in actual practice the aforementioned artifacts often lead to a blurry and low contrast image. As noise is inversely proportional to the square root of the radiation dose, images with less noise can be achieved by increasing the current. However, in clinical practice it is often not desirable to subject patients to an influx of un-necessary radiation.

Recently with the advancements in computational power, iterative reconstruction techniques have been created that are able to mitigate some of the noise associated with the multi-detector computed tomography [47]. These reconstruction techniques are primarily derived by creating first applying a filtered Fourier back projection to the raw data. As the filtered back projection is an approximate approach, a discordance can then be generated between the master image and the current projection. The difference is used to derive an updated projection and thus a slightly corrected projection image. This process is then repeated until convergence.

This approach though time consuming has been shown to greatly improve the specificity of the output image in comparison to standard filtered back projection (FBP) techniques [48].

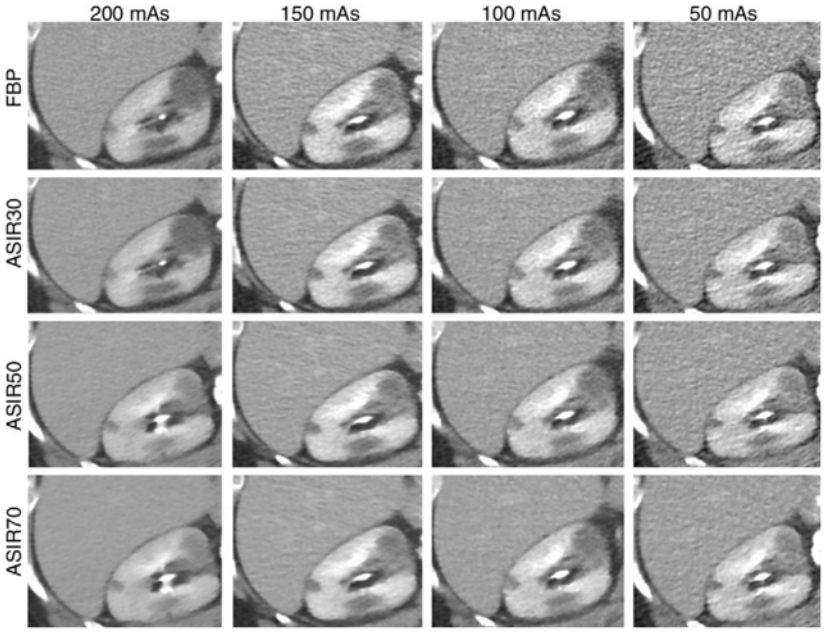

Fig. 2.13 Comparison of the specificity of the image with standard filtered back projection and varying algorithm iteration. [48]

With modern computational enhancements emerging filtering techniques have arisen that hope to significantly reduce the noise present in the images without causing a significant increase in computational time. Deep learning computed tomography unlike iterative back-projection, leverages the use of a trained network on a similar set of projection images Fig.2.14 [49].

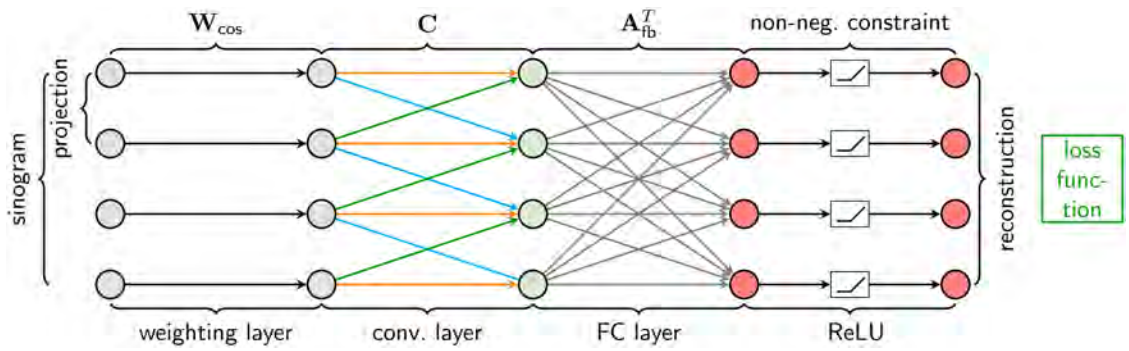

Fig. 2.14 Fan beam architecture for deep-learning computed tomography. Green nodes represent intermediate results in the volume domain and red nodes intermediate results in the projection domain. The color of the nodes represent weight sharing. [49]

Similar pre-determined topologies are fed into the model to first develop a rhobust set of weights that not only describe the general character of the image, but also the nuances in the noise reduction also. Once developed, the model can be deployed on similar but un-seen input geometries yielding in some cases superior reconstruction quality in a fraction of the time of traditional iterative back-projections or filtered back-projections [50, 51].

Deep learning has also had a significant impact in the area of limited angle projections. For clinical applications, a large number of angular samples is not possible due to the increased patient exposure. So far many interpolation/extrapolation methods have been proposed to restore some of the missing information in the image [52–54]. Some methods are based upon the Papoulis-Gerchberg algorithm, which is popular for extrapolation of band limited signals [55]. Other methods are based upon the widely established Helgason-Ludwig consistency conditions, which infer volumes from neighboring values [56].

Recently it has been shown that sparse angle tomography as low as $\pm 10°$ can be reconstructed with machine learning based methods to a high enough fidelity for correct diagnosis [57]. Wurfl et al. [49] proposed a neural network to learn the compensation weights for limited angle data, with other methods such as U-Net achieving impressive results from small scan ranges as low as 120° Fig.2.15 [58].

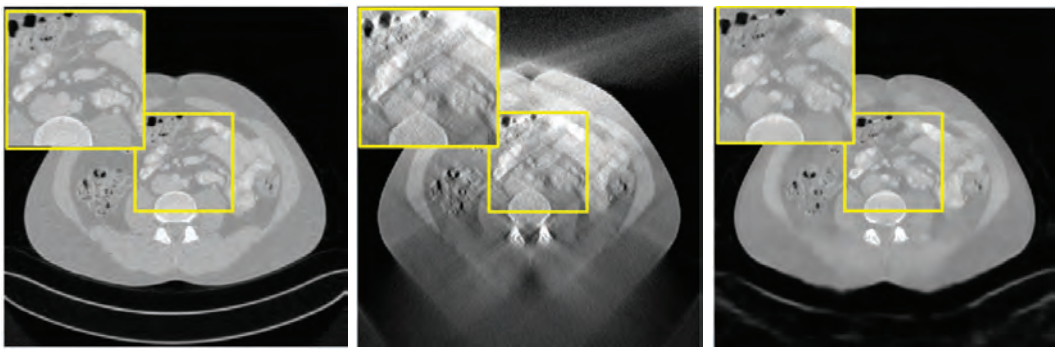

(a) (b) (c)

Fig. 2.15 Reconstruction results of U-net over a 120° scanning geometry. (a) Ground truth image (b) Reconstruction via filtered back-projection (c) U-Net reconstruction. [58]

Chapter 3

Methodology

3.1 Projection Algorithm

The projection algorithm initially resembles that of a traditional DLP or SLA slicing algorithm where the input geometry is represented as a 3D voxel array, that is an array which describes a set of voxels (cubes) that sit inscribed with the surface of the model. The size and number of these voxels is what intuitively describe the resolution of the projected image that we are trying to create. As a voxel loosely resembles that of a three-dimensional pixel, incremental z-slices through the voxel array describe the 2D dimensional cross sections of the model, where the slice height is equal to the thickness of the voxel in the z-direction.

In our case, these two-dimension cross sections of the input model as represented as a binary matrix, with the presence of material being represented by a '1' and the absence of geometry being represented by a '0' Fig. 3.1. This binary representation enables trivial analysis of the cross section via the radon transform and inverse radon transform that is imperative to the projection algorithm. Traditional slicing algorithms such as those used in DLP printing would seize at this step and produce geometry by incrementally exposing each cross sectional image. However, this approach differs significantly, as the generated projections not only have to encompass the topology of the input mesh, but the density as well. In addition to the density, as images are exposed not parallel to the z axis, but instead orthogonal, we need produce projections that contain a holistic view of the model, not just a cross-sectional one. To achieve this, additional computations need to be conducted on the objects cross sections.

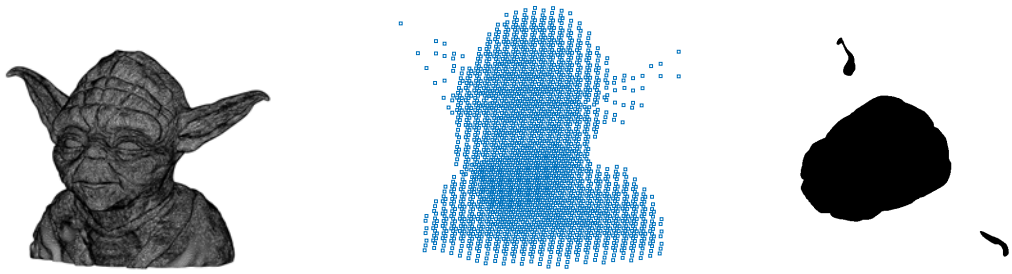

(a) Input yoda mesh (b) Low resolution voxel representation (c) Cross section of voxel array

Fig. 3.1 Process flow representation showing how the target mesh is taken from the 3D representation into its constituent two-dimensional arrays

Lets consider a single two dimensional slice of the object denoted as δz, which represents the cross sectional view of the object at a given z increment. For this slice, volume is represented by the presence of a '1', with the absence of material represented as a '0'. Now for each planar angle θ through this volume we compute the radon transform which represents the line integral through the volume at the representative angle θ.

$$P_\theta(t) = \int_{-\infty}^{\infty} \int_{-\infty}^{\infty} f(x, y)\delta(x \cos\theta + y \sin\theta - t)dxdy \tag{3.1}$$

This transform produces a intensity map that describes essentially the density of the object at a given planar angle. To describe the full picture of the cross section, this process is repeated for incremental angles around the cross section which results in a complex function that describes the through thickness intensity of the slice at a given angle $R(I, \theta, \delta z)$. To reconstruct this slice via the radon transform the Fourier slice theorem can be derived by taking the one-dimensional fourier transform of the radon parallel projection and noting that this is equal to the slice of the two-dimensional Fourier transform of the original object. Therefore, based on this property it is possible to estimate the object by simplify performing the two dimensional inverse of the Fourier representation produced by this technique.

First consider the two dimensional Fourier transform of the object as being described as.

$$F(u,v) = \int_{-\infty}^{\infty}\int_{-\infty}^{\infty} f(x,y)e^{-j2\pi(ux+vy)}dxdy \tag{3.2}$$

likewise the projection defined by a given intensity function $P_\theta(t)$, and orientation angle θ, can be defined by its representative Fourier transform is dictated by.

$$S_\theta(w) = \int_{-\infty}^{\infty}\int_{-\infty}^{\infty} f(x,y)e^{-j2\pi w(x\cos\theta+y\sin\theta)}dxdy \tag{3.3}$$

Therefore, by taking representative projections of the object at various incremental angles $\theta_1, \theta_2, \theta_3 ... \theta_k$ and applying the one-dimensional Fourier transform of each of these projections we can determine the values of the function $F(u,v)$ which lie on radial lines through the Fourier domain of the subsequent object Fig. 3.2. Ideally, an infinite number of projections would be taken such that the object could be fully represented in the Fourier domain. Computationally this is not possible, as an infinite number of projections cannot be produced for a given slice through the object, therefore it is clear that the function $F(u,v)$ can only accurately be represented at positions along the radial lines at not for any point in the fourier domain.

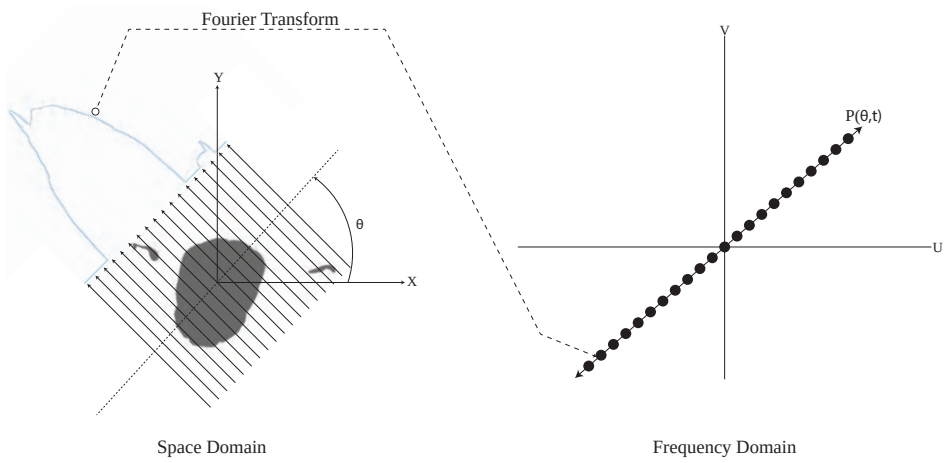

Fig. 3.2 This process highlights how the one-dimensional projections produced by the radon transform and used to construct the two-dimensional fourier domain

This therefore poses a significant challenge in accurately reconstructing the model for two primary reasons. First, as the data is only distributed along the radial projec-

tion lines, data outside of this region would not be represented leading to gaps in the reconstruction. The second issue is due to the method in which the sampling is taken for data in the fourier domain.

From the two-dimensional fourier representation shown above, we can observe that their is a greater representation of low frequency data, than high frequency data, due to the angular sampling method. This poses a difficult problem, as high frequency data is usually represents sharp features such as edges or detail within the model. This under representation of high frequency data, will result in images produced by this technique to appear soft and without contrast.

Therefore, in order for the two dimensional fourier representation $F(u, v)$ to be used effectively, the missing values produced by the fourier slice theorem need to be reconstructed to represent a complete fourier domain. One of the most common methods to solve this problem, is to interpolate these radial lines onto a uniform grid. Nearest neighbor or linear interpolation techniques can then be used to approximate the missing data from the two-dimensional fourier domain. Since the density of the radial points become increasingly more sparse as we move away from the center of the fourier domain, the interpolation error also becomes larger. This implies that their is a greater error with representing high frequency data (sharp features) than that of low frequency ones, which inherently results in image degradation (Figure 3.3).

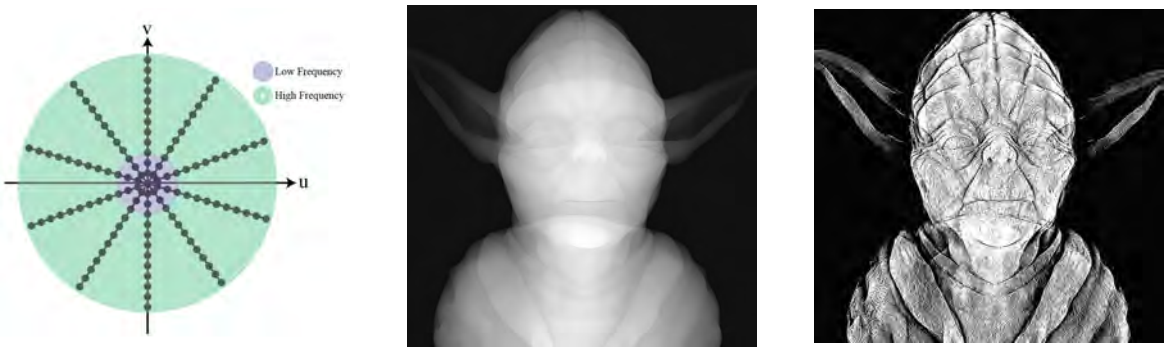

(a) Fourier sampling (b) Unfiltered model (c) Ram-lak filtered model

Fig. 3.3 **(a)** Representation of how the interpolation error in the model increases with the radial distance in the Fourier domain. **(b)** Unfiltered projection of the yoda model, showing reduced clarity in the image due to the under representation of high frequency data. **(c)** Ram-Lak filtered projection data of the yoda model demonstrating how suppression of low frequency noise reveals sharp features.

As this process tends to produce a result that has an over representation of the low frequency data and an under representation of high frequency data a function needs to be applied to correct for this. To achieve this, the most common method is to use a Ram-Lak filter, which is essentially a high pass filter. This filter passes data with high frequency and attenuates the low frequencies. By applying this filtering process to the Fourier representation $F(u, v)$, a filtered fourier representation can be achieved. To convert this representation back to the Fourier domain, a standard inverse fast fourier transform can be used to describe the final cross sectional image.

To achieve the full representative projection of the holistic model, this process is repeated for each incremental z step δ_z, such that a filtered set of projection are produced for any given angular orientation of the model θ and slice δ_z. This can then be presented as a filtered intensity defined as $P(I, \theta, \delta_z)$, where I represents the intensity function for that given through thickness domain. The one-dimensional filtered projection is then incorporated into the holistic projection, where the matrix is represented as $[\delta_z, P(I, \theta, \delta_z)]$ (Figure 3.4).

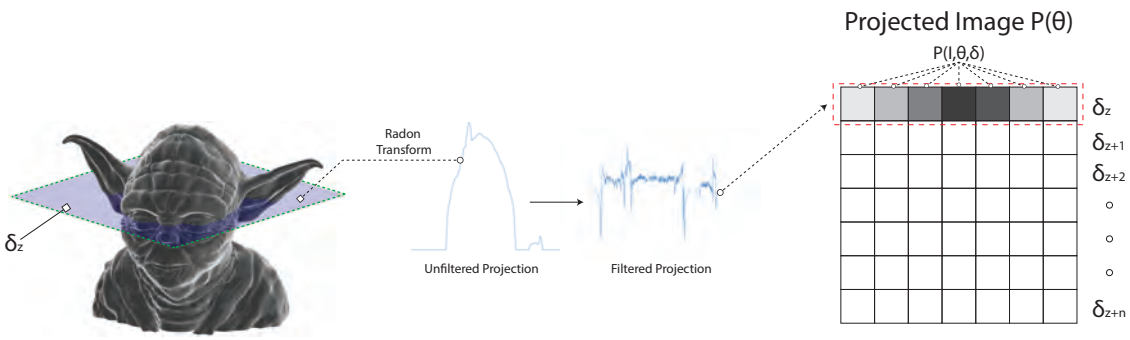

Fig. 3.4 Generalized process of data is extracted from the two dimensional slice, represented as a filtered projection and then inserted into its equivalent projection array

To achieve the final projection image at a given angle θ, this process in then repeated for each incremental slice through the object δ_z such that we produce a matrix of size $\delta_z \times P(\theta)$. To produce a full set of image projections for the model, this process is repeated once again for each incremental angle θ around the object azimuth. These images are then combined into a single video file for printing where the frame rate of the video file dictates the speed at which the resin container rotates.

3.2 Resin Kinetics Model

The purpose of the resin kinetics model is to determine an optimized set of projections such that we only adequately cure the print volume. For this volumetric printing process to work effectively the model needs to ensure that regions are not over or under exposed at this can lead to issues in the dimensional accuracy of parts produced by this process. To achieve this the projections have an additional filtering step which tries to optimize the intensity of each pixel in the image based on resin kinetic information.

First a set of projection images are produced using the projection algorithm described above that will be dictated by $P(\theta)$ where P represents the given projection image at angle θ, with each pixel within this image being described by $P_{ik}(\theta)$. The concept of this method is to observe the equivalent intensity delivered by these projections and adjust the output projections such that they meet a given intensity threshold defined by the degree of cure function.

The classical equation for free radial polymerization in bulk [25] can be used as the model of the system where the parameters k_p and k_t represent the propagation and termination coefficients respectively for our resin system, $[M]$ is the prepolymer concentration, ϕ is the quantum yield and I_a is the absorbed intensity of the source.

$$R_p = \frac{k_p}{k_t^{1/2}}[M]\left(\phi I_a\right)^{1/2} \tag{3.4}$$

As the reaction proceeds and cross linking is formed, the prepolymer concentration will begin to drop at the propagation rate R_p defined as.

$$R_p = -\frac{d[M]}{dt} \tag{3.5}$$

Therefore, we can finally define the degree of cross linking (DOC) as the radio of cross links formed to available reaction sites. Therefore, the degree of cure can be written in terms of the ratio of the initial prepolymer concentration and the final prepolymer concentration.

$$DOC = 1 - \exp\left(-\frac{k_p}{k_t^{1/2}}\left(\phi I_a\right)^{1/2} * t\right) \tag{3.6}$$

From Equation 3.6 we can see that the degree of cure for the polymer is not only dependent on the exposure time but the intensity as well. To ensure that we are adequately curing the resin volume we can compare the theoretical exposure over time delivered to the volume, in addition to the cumulative image intensity. As this process quickly becomes complex to optimize for both exposure and intensity, a simple case has been considered where a fixed print duration is set and the intensity is optimized.

To achieve this outcome we consider a single pixel in the projection array which contains a gray scale value between 0 and 1. Assuming a linear distribution of energy for the projection system, we can associate a power output for this given pixel to be proportionally bound by the maximum output of the projector divided by the total number of pixels. Therefore, the intensity for a given pixel $I_{ik}(\theta)$ can be written as a function of the output power W, the gray-scale value of that given pixel $P_{ik}(\theta)$. Where i,k, are the number of pixels in the x and y directions respectively.

$$I_{ik}(\theta) \propto P_{ik}(\theta)\frac{W}{ik} \tag{3.7}$$

Consider a single pixel which can now be defined by its approximate intensity $I_{ik}(\theta)$, where θ now not only represents the given angular projection but also some period in time t. We can now determine for a given pixel, the cumulative energy transferred into the volume as a function of time by taking the summation of the pixel intensity across all angular domains.

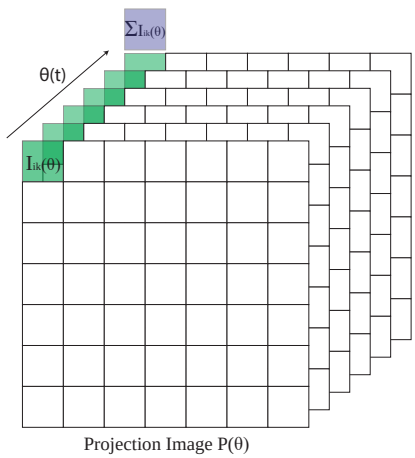

Fig. 3.5 For each pixel within the projection array the approximated intensity is summated to determine the total energy delivered by that individual pixel. This is compared against the target intensity and adjusted accordingly.

$$\mathbf{I_{ik}} = I_{ik}(\theta_1) + I_{ik}(\theta_2) + I_{ik}(\theta_3)...I_{ik}(\theta_n) = \sum_{n=0}^{n} I_{ik}(\theta_n) \tag{3.8}$$

As the critical cumulative intensity can always be determined for a given fixed exposure time, the intensity produced by Equation 3.7 can be compared against the target output defined by Equation 3.6. By independently increasing or decreasing the gray scale value in each array and thereby changing the exposure dose, an optimized set of projections can be determined such that the cumulative intensity matches that of the target intensity. To achieve a full set of optimized projections, this approach is repeated for each pixel in the projection array, such that an optimized image is achieved that critically cures the volume.

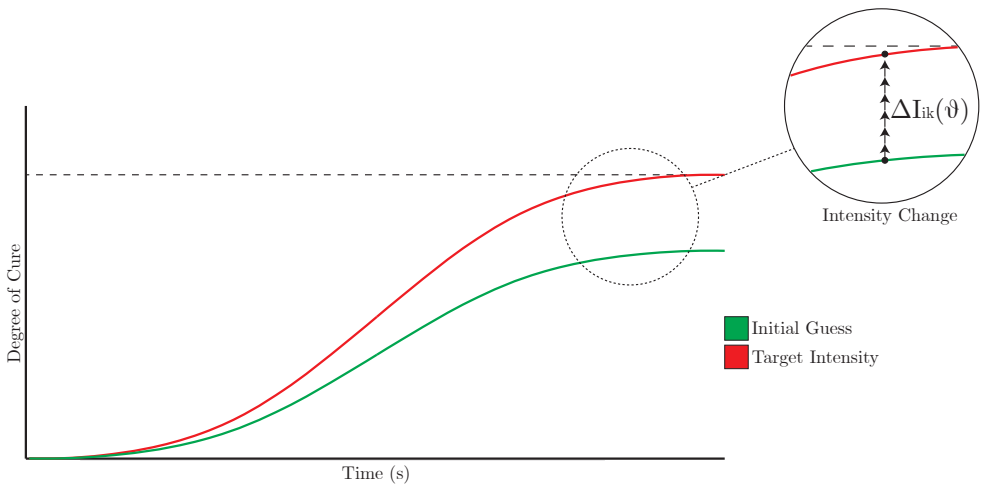

Fig. 3.6 The degree of cure is plotted for the initial projection intensity. For each incremental angle the difference between the target exposure and the current exposure is determined. The pixel intensity is then scaled proportionally based on this difference, to achieve an optimized projection.

3.3 Biaxial Thresholding

One additional consideration that is required for reliable printing is for transverse thresholding to be applied to the final image. To understand the importance of this, lets first consider a single point p located at the extremities of the build volume. If we evaluate this point from the view of the radon transform, we can see that this point can be easily reconstructed by subsequent projections, as their is no attenuation acting on the beam path.

However, in reality the light propagating through the medium experiences significant attenuation as the volume rotates. For regions close to the center of the container, light rays remain in contact with the geometry for the duration of the print time. Whereas, as parts move out radially from the center of the container they experience a dose maxima proportional to $r_p sin\theta$ as shown in Fig. 3.7. In general, this leads to regions close to the wall boundary experiencing a lower cumulative dose via subsequent projections and thus are reconstructed behind central regions.

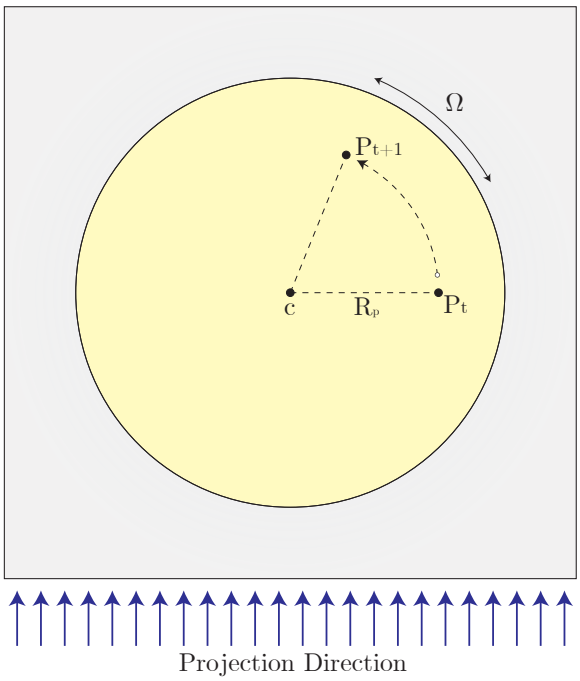

Fig. 3.7 Rotational intensity variation of boundary points within the volume.

To tackle the challenge, a transverse threshold is applied to aid in developing these exterior regions without over exposing central regions. To achieve this, a parabolic distribution is applied to the image, such that the intensity of exterior regions are increased relative to the center of the volume. As the degree of cure is not linearly proportional to the intensity map, a parabolic distribution was chosen to approximate the delivered dose. Note this assumption is assuming that the generated geometry is significantly smaller than the container dimensions. In cases where the geometry exceeds this constraint, thresholding may need to be significantly non-linear to account for the low through thickness attenuation at the extremities of cylindrical build volumes.

In most cases this distribution ranged from 100% at the exterior of the image, down to 45-60% at the center of the image to still ensure that central topologies are reconstructed in approximately the same time. Fig. 3.8 highlights how regions near the center of the image are truncated to preserve geometry.

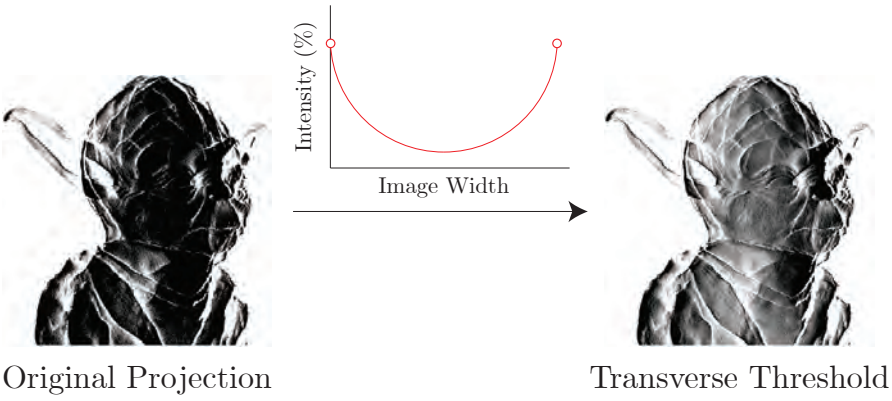

Fig. 3.8 Effect of transverse scaling on the output of the yoda target geometry.

One additional consideration that was taken when reconstructing target geometries was the influence of part cross-sectional area. As the radon transform is proportional to the cross-sectional area of the part, cross-sections with a higher area tend to cure exponentially faster due to the increase in intensity of these regions. To correct for this, some geometries were normalized based on the average cross section of the part. This ensures that even regions with small cross-sections and thus small line integrals through the volume, are still represented in the curing cycle without causing detrimental over-curing in other regions of the volume.

3.4 Reconstruction Algorithm Flowchart

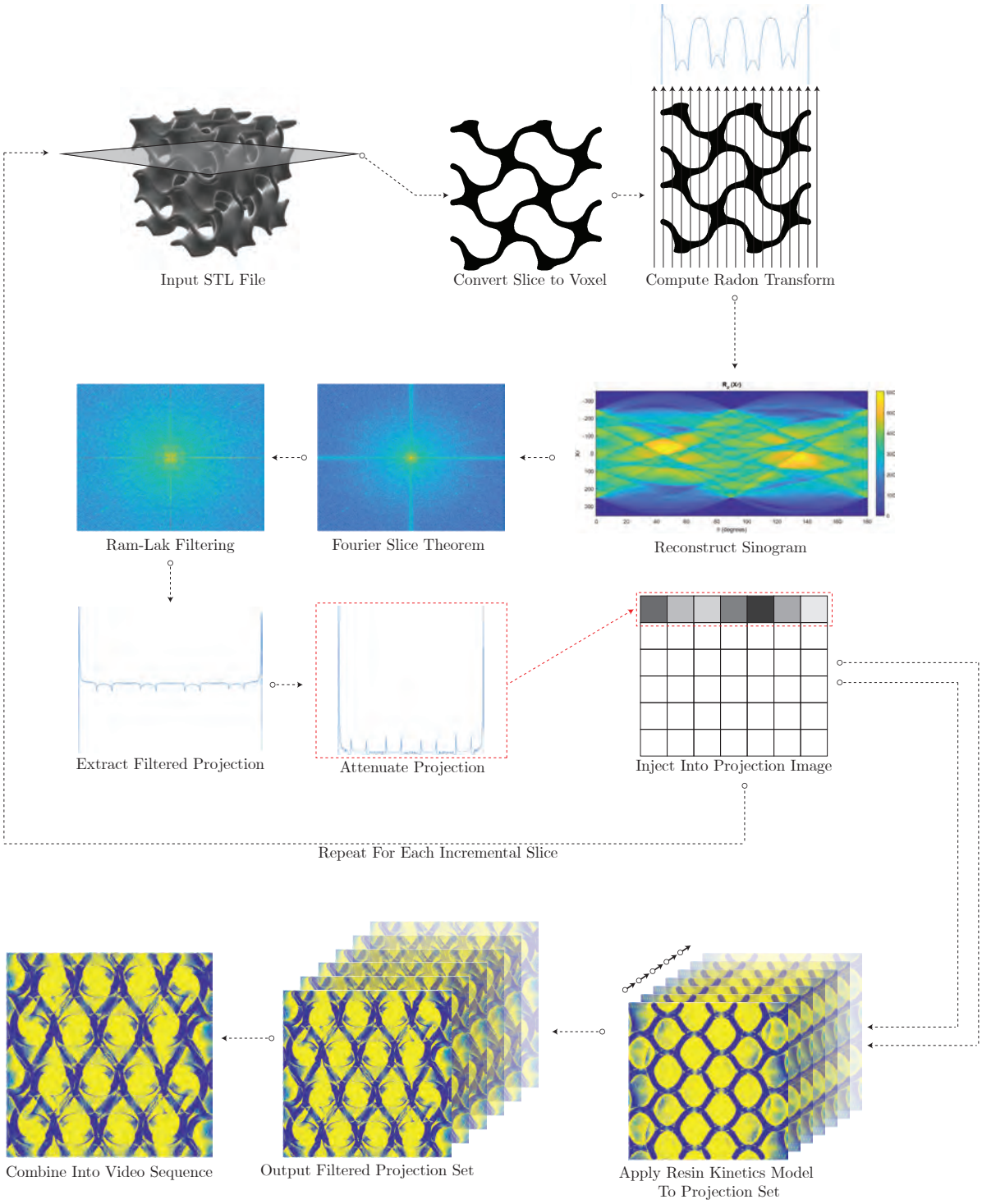

3.5 3D Reconstruction

Validation and optimization of the projection algorithm is key in ensuring accurate and precise reconstruction of the target geometry. However, performing this optimization procedure physically in the build volume is both time consuming and highly subjective. To address these issues, a reconstruction engine was created to interpret given projection data and produce a representative 3D model as well as a accuracy score which characterizes the effectiveness of these projections to produce required topology.

Consider a single projection image I being defined as a grey-scale matrix containing $m \times n$ pixels. If we first consider a single pixel in this array we can project a vector $V(\gamma, I, m, n)$ which is orthogonal to the image plane and has a pixel intensity weight γ. If we repeat this process for each pixel in the image we produce a single vector image at a given angle θ. This process is then repeated for each image in the data set, producing an array of intersecting vectors with each vector carrying intensity information based on its individual grey scale value and a direction defined by the image plane Fig 3.9.

This in turn creates a complex point cloud, with each node being represented by both an (x,y,z) coordinate and a unit-less intensity value based on the sum of its vector weights.

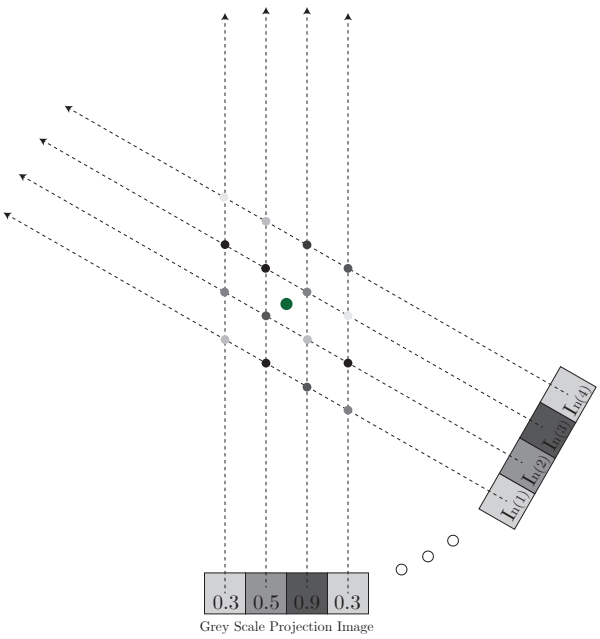

Fig. 3.9 Illustration of how the target geometry point cloud is reconstructed from a series of projection images.

This intuitively produces an extremely incoherent point cloud, as points are produced exterior to the target geometry by scatted projections. In reality, these scatted projections do not cause curing as they are unable to overcome the cumulative intensity threshold required to initiate curing. To mimic this behavior, the point cloud undergoes an additional thresholding that removes unwanted nodes that are under the required threshold dictated by the resin kinetics model. Nodes that are identified as partially or fully cured by the kinetics model are represented by a colour map. Using a marching cube algorithm, the filtered point cloud is interpolated and converted to an STL file which represents the cumulative dose produced by the filtered back projections.

Measuring the accuracy of the reconstruction is difficult to achieve when the model is in 3D, to negate this, the produced STL file is first re-vocalized back into its constituent slices and compared against the input STL at the corresponding slice intervals. For comparison the input and output slice is computed using the Jaccard Index which measures intersection over union of the two-binary fields. This produces a confidence coefficient between 0 and 1 depending on the similarity of the images Fig 3.10. This process is repeated for each incremental z slice through the volume, and the lowest Jaccard Index is taken for comparison.

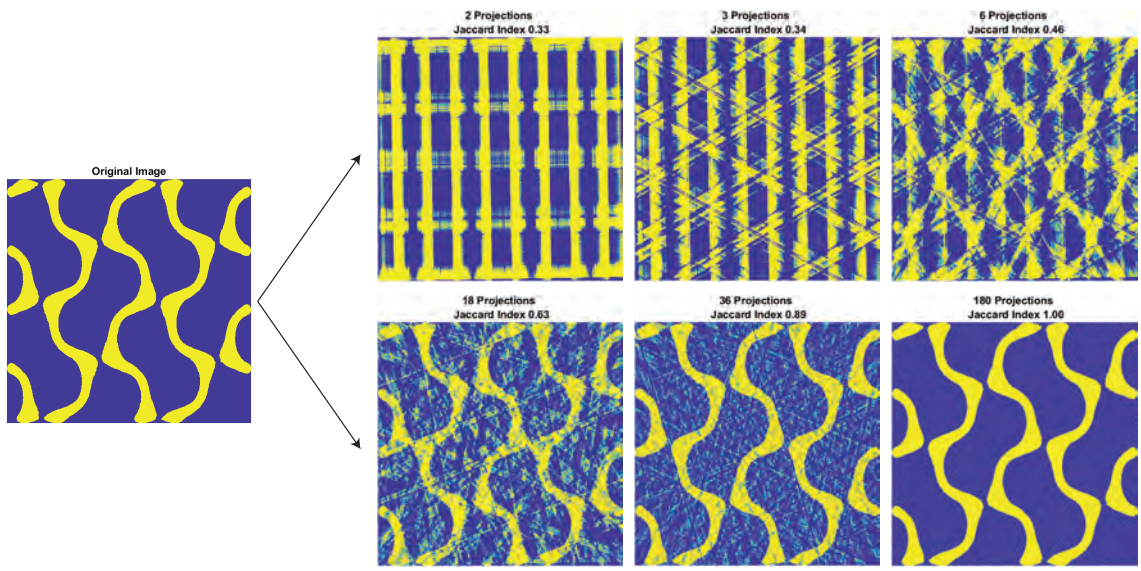

Fig. 3.10 Evolution of the jaccard index for various projection angles of the Gyroid geometry.

3.6 Mechanical Design

3.6.1 Volume MK1

To explore the implications of volumetric printing and to validate the aforementioned tomographic algorithm an initial mechanical printing system was developed. This system borrowed some consideration from previously developed work [12] by leveraging a standard desktop projector as the projection source. The system consisted of a Epson EH-TW5600 desktop projector, a A4 fresnel lens sheet, index matched resin tank and a custom designed horizontal lifting gantry Fig. 3.11. The gantry and subsequent resin container mount were both connected to a NEMA 17 stepper motors, with the resin container being driven by a TB6600 micro-stepper driver to enable a greater angular resolution.

To produce a somewhat coherent and collimated beam path, a fresnel lens was placed infront of the projector to collimate the fanned beam produced by the projector. The projected beam was sent into a square glass container containing parifin oil which has a refractive index close to that of the resin mixture. The purpose of this step is to minimize the cylindrical lensing effects caused by the convex nature of the printing container. The projected image was produced by a custom MATLAB script and sent to the projector by the integrated HDMI connection.

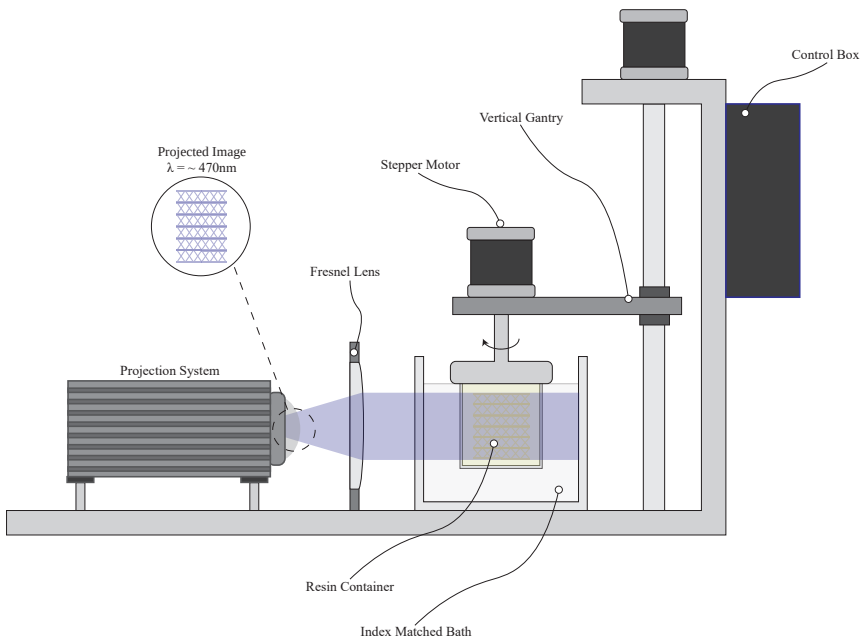

Fig. 3.11 General component and optical layout for the Volume MK1 printer.

3.6.2 Volume MK2

As mentioned previously one of the inherent challenges of using off the shelf digital desktop projectors is that without removing the optical train, the images produced suffer from great spacial divergence, even over the short focal depth of the build volume. As the developed algorithm assumes the basis of parallel ray projection, diverging beams offer a significant challenge to recreate complex topologies.

Previous high resolution volumetric printing methods leveraged the use of DMD/DLP technology as the primary mechanism for spacial light modulation [15].Though this method offers some significant benefits over the current approach, most notably in regards to image resolution and light efficiency, the technology is extremely expensive due being exclusively licensed by Texas Instruments. The approach used in this work shown in Fig. 3.12 takes inspiration from the low cost stereo-lithography community, most notably Mask Stereo-lithography (MSLA) that uses a LCD display as a masking medium to produce pattered cross sections of the target geometry [59]. This approach offers a significantly cheaper alternative to DLP however does require a higher power density due to the relatively low transmittance of liquid crystal displays (LCD) [60].

As the LCD display essentially acts as masking medium to the light source, to produce a collimated image a highly collimated and uniform backlight needed to be produced. To achieve this a high power 15W blue laser diode (450nm) was coupled to a $150\mu m$ x $150\mu m$ square core optical fiber (Thorlabs FP150QMT) using a custom designed 3D printed micro-stage. The purpose of the square core optical fiber is to first clean up the multi-mode aberrations seen in low cost diode lasers and second produce a somewhat square beam profile to closely fit the LCD display. To further improve the optical efficiency of the setup two orthogonal cylindrical lenses of different focal lengths were used to reshape the square profile produced by the fiber into the 16:9 rectangular shape needed for the LCD panel.

To improve the collimation of the back projection a 4f spacial filter was used to remove any unwanted high order diffraction in the fourier plane. To achieve this, first the output beam from the two orthogonal cylindrical lenses were re-orientated due to geometry constraints within the chassis enclosure using a pair of 90° prisms. The beam of light is then applied to the 4f spacial filter where a variable aperture is placed in the fourier plane of the beam path. To filter out any unwanted high-order diffraction, 4 razor blades were mounted onto a cylindrical aperture with magnets. The magnets

enable the razor blades to move somewhat freely enabling filtering in both the x and y direction. The filtered beam profile is then expanded and collimated through a 5.5" lS055R1SX04 1440x2560 liquid crystal display. In this setup the back-light of the display was removed to enable secondary light to pass through the sub-straight.

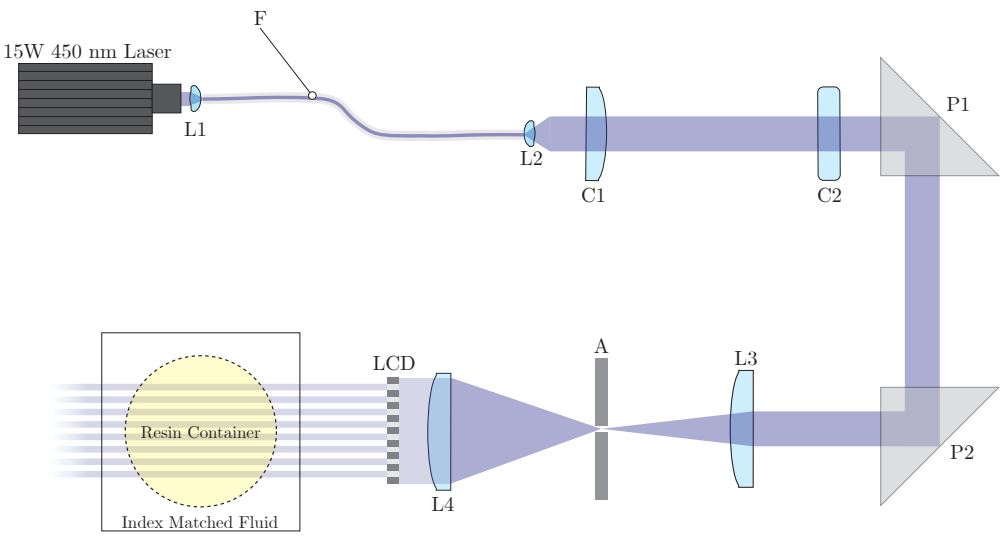

Fig. 3.12 General optical layout used for the Volume MK2. L1: 3.1mm aspheric lens; F: Thorlabs FP150QMT $150\mu m \times 150\mu m$ square core optical fiber; C1: 250 mm cylindrical lens; C2: 300 mm cylindrical lens; P1: 90° prism; P2: 90° prism; L3: 150 mm plano-convex lens; A: variable square aperture; L4: 250 mm plano-convex lens.

To aid in ease of use of the of removing the cylindrical container from the index matched fluid a vertical gantry system was used to place and remove the building volume into the beam path. The resin container was rotated using a DC motor with an encoder to guarantee a precise and controlled rotation of the volume and was rotated between 6 - 12 rpm depending on the geometry type.

Control of the printer itself was controlled by an Arduino Uno running a state machine of all possible printer commands. These commands were then executed by the Matlab GUI by simply sending serial commands over USB to the Ardunino Uno.

3.7 Resin Development

Due to the self supporting nature of volumetric printing, traditional resin systems used for stero-lithography cannot be used due to their low viscosity. As the density of the material changes slightly during the print cycle, this infers a buoyant force on the partially cured resin Fig. 3.15. Therefore, sedimentation of the volume during the sub-minute print duration sets specific constraints on the resins dynamic viscosity. The sedimentation speed v for on object section L whose cured density is defined as ρ_{solid}, initial density ρ_{liquid} and dynamic viscosity η can be written as [61].

$$v = \frac{(\rho_{\text{solid}} - \rho_{\text{liquid}})\, g L^2}{18\eta} \tag{3.9}$$

Therefore, by limiting the vertical resolution of the sedimentation to be $< 50\mu m$ and defining a prepolymer solid and liquid density, we can determine a minimum dynamic viscosity required for volumetric printing. However, in our case as we are using a prepolymer where the differences between the solid and liquid densities are minimal, which enables printing within a 30s window without any significant detrimental effect. Furthermore, as the printing system does not infer any mechanical motion within the printing volume, we can therefore use extremely high viscosity resins that are less prone to sedimentation issues. These high viscosity resins would traditionally be difficult to print, due to the motion caused by the build platform in currently available light based AM methods.

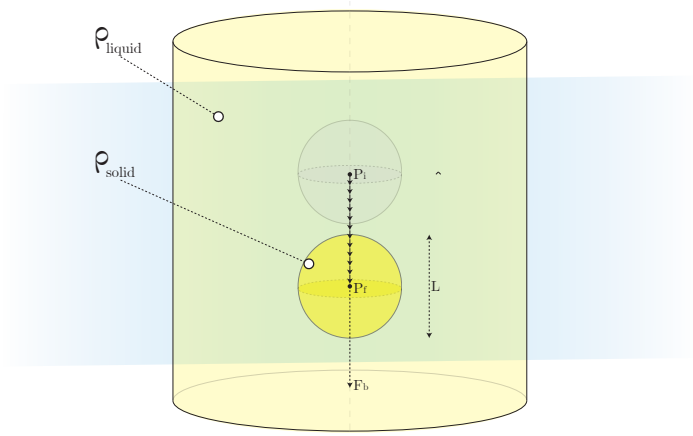

Fig. 3.13 As the degree of cure increases within the resin volume, changes in the resin density cause significant displacement due to a buoyant force. These displacements can be minimized through the use of high viscosity resin systems.

Additional constraints are set on the optical requirements of the resin system, as light needs to fully propagate through the volume to cure all regions adequately. By knowing the absorption coefficient of the photo-initiator α for a given wavelength, we can adjust the required photo-initiator concentration c, such that the optical attenuation l is greater than the length of the printed object.

$$c = \frac{1}{\alpha l} \tag{3.10}$$

It is hypothesized that this will ultimately limit the size of the printed objects as the low photo-initiator concentration required for large objects will result in poor polymer yield and mechanical properties. To achieve larger objects via volumetric printing, a resin system needs to have high reactivity and low absorption, which is opposite to most SLA resin systems that exhibit low reactivity and high absorption.

The resin system chosen for this application is a two part resin consisting of a 3:1 ratio of poly(ethylene glycol) diacrylate (PEGDA) and bisphenol A glycerolate (1 glycerol/phenol) diacrylate (BPAGDA). This system exhibits extremely high viscosity to minimize sedimentation effects during the printing cycle. To achieve polymerization via the 450nm blue laser, a type II photo-initiator system consisting of Camphorquinone (CQ) and ethyl 4-(dimethylamino)benzoate (EDAB) were added to the polymer mixture in a 1:1 ratio, such that the concentration of CQ in the polymer mixture was 0.07% w.t.

Though the photo-initiator system primarily used for this work was CQ + EDAB, some other photo-initiators were also explored with varying results. Phenylbis(2,4,6-trimethylbenzoyl)phosphine oxide) also known as Igracure 819 was also used for some initial testing due to the system already being readily available. Though this system did obtain some favorable results, the curing was highly unpredictable due to the low absorbance in the blue light spectrum. For ultra-violet curing however due to its high absorbance we suspect that Igracure 819 would be a perfect match and significantly more cost effective than the CQ + EDAB mixture.

3.8 Resin Fabrication Methodology

Due to the highly viscous nature of PEGDA, accurate mixing of this resin can be challenging. To assist with this, PEGDA was first heated to 70°C within an oven to significantly reduce the viscosity of the resin. The mixture of PEGDA and BPAGDA was then combined into a mechanical mixer and mixed at low speed to minimize incorporation of air into the polymer. This was repeated until the two mixtures were fully incorporated. Though this method aims to minimize the inclusion of air into the polymer, due to the viscous nature of the resin, air will always be present within the mixture. This causes significant optical obstruction, thus to remove these bubbles the mixture is then held under vacuum to evacuate any trapped air.

To ensure that the resin is fully incorporated, three 1mL samples are taken from the mixture at various points within the volume and weighed to ensure that the density of the resin matches the theoretical density of the mixture ($\rho = 1.165\ g/mL$). The resin was then stored in an airtight clear container prior to adding the photo initiator mixture.

As the print volume for this printer consists of a clear 70mL vial, all resin mixtures were made within this volume to reduce trapped air when transferring between containers. First a 70 mL container was filled with polymer mixture and submerged in a 80°C water bath to decrease the resin viscosity. Next an eppendorf filled with a few drops of isopropanol is combined with the CQ and EDAB in a 1:1 ratio by weight, such that the concentration of CQ within the resin is 0.07% w.t. As CQ is a rough powder, the mixture was then vortexed for 1 minute to break up the powder within the isopropanol solution. This mixture is then combined into the resin mixture and stirred thoroughly. As CQ takes a few minutes to dissolve into the resin solution, this mixture was sat in the water bath for an additional 20 minutes to ensure that CQ was fully dissolved. This mixture was then removed and sat to cool in a dark place prior to use.

3.9 Regeneration of Resin

Traditionally, the inclusion of oxygen within the print volume is a negative factor as it inhibits the polymerization process by requiring that the concentrated oxygen first be depleted before polymerization can occur. However, in our case this inclusion of oxygen enables light to pass through the volume without instantly causing it to cross link. In regions such as the printed part, the cumulative light dose is high enough to exceed this oxygen depletion threshold and initiate curing, with regions around the printed part still having varying levels of oxygen due to a lower light dose. This proposes a challenge when directly reprinting this already exposed resin. As there are varying levels of oxygen within the volume, the oxygen depletion will therefore not be directly linked to the applied light dose, but instead dependent on the previous light dose as well.

Thus, to achieve accurate reprinting of already exposed resin, the oxygen content needs to be re-equalized to ensure a uniform oxygen concentration throughout the resin. This is achieved by allowing environmental oxygen to re-diffuse back into the polymer mixture. For this the spent mixture was poured out onto a petri dish submerged in a shallow water bath heated to 80°C. The petri dish was chosen such to maximize the surface area and minimize the depth of the resin, to maximize oxygen diffusion. The resin mixture was then left for 1hr in a dark oxygen rich environment. After 1hr the material was poured back into a container and let to cool for reuse.

3.10 Part Post-processing

As volumetric printing aims to deliver only an adequate amount of light to the volume to polymerize the structure, parts produced tend to be soft directly after printing. Just like any other resin based printing process parts require post curing to achieve their desired mechanical strength. Directly after printing objects were first washing in an isopropanol bath to remove any uncured resin from the surface.

Due to a high concentration of ambient oxygen at the model's surface curing the models in air will not yield a very desirable result, often leading to the surface remaining considerable tacky to the touch. To alleviate this problem, the printed models were placed in a vacuum chamber during the curing process to minimized the oxygen inhibition at the model surface. Alternatively, the part can be submerged in water, however this often led to surface defects being present on the cured model.

3.11 Volumetric Exposure Time

To determine the minimum exposure time required to solidify the geometry we can consider a general point P in the rotating container. This point lies at a radial distance c from the center of the container which has a radius defined by R. Assuming that the absorbance of the index matched fluid does not interfere with the dose delivery. The propagation distance w achieved by the pre-polymer material at location P within the volume can be defined by.

$$w = \sqrt{R^2 - c^2 \sin^2 \theta} - c \cos \theta \tag{3.11}$$

Lets define T_v which is the time taken for the cumulative volume dose D_c to fully cure point P located within the volume. By assuming that the time for one revolution of the build volume is significantly less than T_v, we can define that curing occurs when.

$$D_c = \frac{T_v}{2\pi} \int_0^{2\pi} B_v \mathrm{d}\theta \tag{3.12}$$

Where B_v define the photon absorption rate defined by $B_v = \alpha_v \Phi_{0,v} e^{-\alpha_v w}$. Therefore, substituting into the above equation yields the volumetric print time defined by.

$$T_v = \frac{2\pi D_c}{\int_0^{2\pi} B_v \mathrm{d}\theta} = \left(\frac{D_c}{\Phi_{0,v}}\right) \frac{2\pi}{\alpha_v \int_0^{2\pi} e^{-\alpha_v w} \mathrm{d}\theta} \tag{3.13}$$

By inspection we can determine that the minimum print time will occur when $\alpha_v R = 1$, which offers significant constraint to the formulation of photosensitive material. Therefore, we can derive the minimum print time by setting the maximum penetration depth equal to the radius of the containment, $w = R$ and $\alpha_v R = 1$, thus.

$$T_{v,\min} = \left(\frac{D_c}{\Phi_{0,v}}\right) \frac{2\pi}{\frac{1}{R} \int_0^{2\pi} e^{-1} \mathrm{d}\theta} = \left(\frac{D_c}{\Phi_{0,v}}\right) eR \tag{3.14}$$

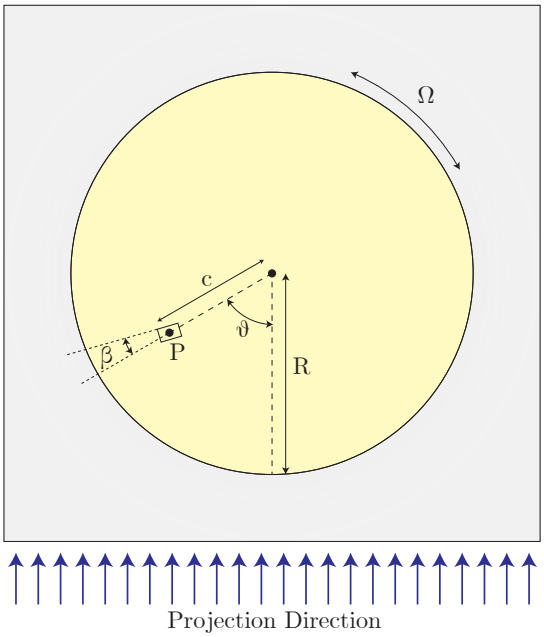

Fig. 3.14 Geometric nomenclature for the theoretical development of the exposure time for volumetric printing

3.12 Beam Divergence

The aforementioned algorithm assumes that the light rays used for reconstruction are perfectly parallel, however in reality this tends to be not the case. This challenge is one of the factors that limit the achievable resolution by volumetric printing, as it dictates the minimum voxel size within the volume.

To determine the minimum voxel size lets assume that the build volume has a length of L_b which in this case is equal to the diameter of the volume. With the minimum width of the voxel dictated by L_{vox} which is the size of the voxel in the center of the volume after being imaged by the LCD display. The goal of this optical setup is to limit the theoretical divergence of the beam i.e produce a highly collimated light source. If we assume that the divergence of the beam expands to at most $(1+p)L_{vox}$, where p describes the divergence of the beam over the build volume. In this case we can determine the divergence angle to be $tan\theta = PL_{vox}/L_b$ with the numerical aperture of the beam to be $NA = nsin\theta \approx npL_{vox}/L_b$.

Assuming that the LCD display provides light for all sub-voxels we can determine the expansions factor p to be defined by $L_s NA_s = npL_{vox}$. Where L_s represents the size of the optical fiber, NA_s is the numerical aperture of the fiber.

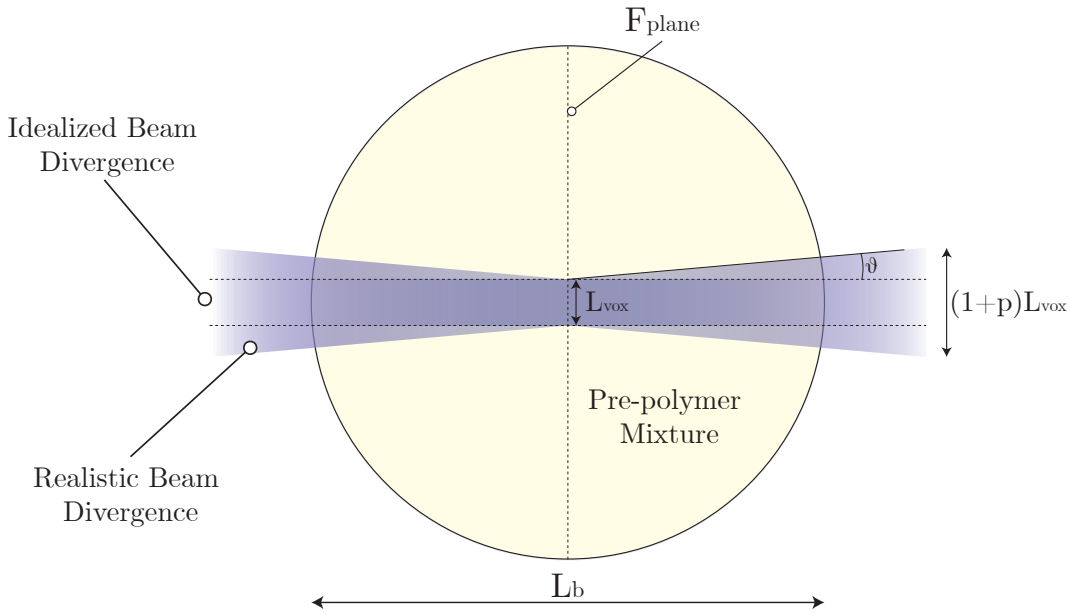

Fig. 3.15 Geometric nomenclature for the theoretical development of the image divergence present in volumetric printing.

In our case the 2K LCD display provides a pixel resolution of $L_{vox} = 42\mu m$ with a numerical aperture of 0.39, fiber core of $L_s = 150\mu m$ and a polymer index of refraction of 1.49. We can determine that the divergence coefficient p to be 93.4% which represents that the voxel will be $42\mu m$ at the center of the volume and $81.2\mu m$ at the edge of the build volume. Though this gives an approximate spacial resolution, other effects such as interracial scattering and chemical diffusion of the polymer will limit this resolution even further.

3.13 Spin Up to Steady State

For the printing process to be successful all points within the volume must have the same angular velocity prior to printing to negate mixing effects of partially cured material. The spinning up of a body to steady state is a known problem in fluid mechanics referred to as the "rigid body' condition and is primarily driven by the geometry of the vessel, the angular velocity of the container and the kinematic viscosity of the fluid.

In the case of higher velocities, lower viscosities and or larger container volumes, the spin up time is governed by the outward radial secondary flows which are caused by centrifugal forces and characterized by the Ekman time [62].

$$T_{Ekman} = H\nu^{-0.5}\Omega^{-0.5} \tag{3.15}$$

Where H defines the height of the container parralel to the rotation axes, ν is the kinematic viscosity of the fluid medium and Ω describes the angular velocity of the container. In our case due to the relatively small dimensions of the build volume, the spin up time is primarily dominated by radial diffusion and not radial secondary flows. This can be described by the following relation [63].

$$T_{diffusion} = R^2\nu^{-1} \tag{3.16}$$

By applying this to our setup we can determine that the spin out time is in the order of a few fractions of a second. In our case as our kinematic viscosity is so high, consolidation of the volume is almost instant. However, for thinner fluids or greater build volumes, some care needs to be taken to ensure the homogenization of the volume prior to printing.

3.14 Overprinting Algorithm

One interesting implication of volumetric printing, is the ability to produce geometry in/or around already existing parts. This has the possibility to produce fully assembled geometries without the need of supporting elements. However, overprinting tends to cause some significant reconstruction challenges due to the shadow occlusion formed by the 'dark-side' of the obstruction.

As large parts of the reconstruction can be blocked or subdued due to the significant reduction in intensity in these areas, some alteration to the forward model needs to be considered to ensure that the volume is voxelized concurrently. Given a specified printing volume with a strictly convex occlusion, it is always possible to find a semi-circle to exposure every point. We can thus use half angle exposures of various points throughout the volume, such that the combination of these exposures enables reconstruction of the occluded regions. Due to the symmetry in the radon transform we can thus define this over a 180-degree semi-circle as:

$$f(\boldsymbol{r}) = \int_{\theta=0}^{2\pi} g(\boldsymbol{r} \cdot \hat{\theta}, \theta) d\theta = 2 \int_{\theta=\theta_0}^{\theta_0+\pi} g(\boldsymbol{r} \cdot \hat{\theta}, \theta) d\theta \tag{3.17}$$

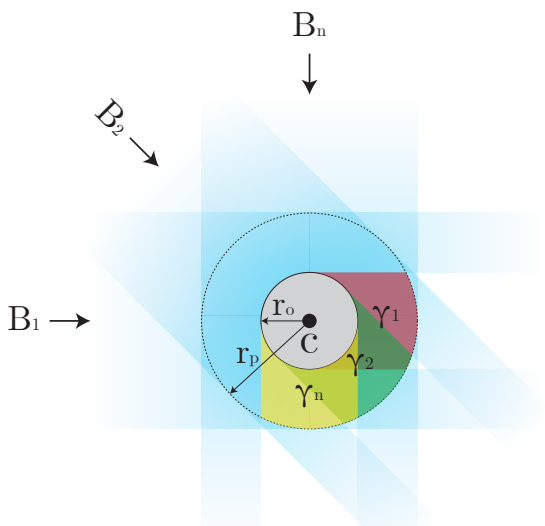

Fig. 3.16 Illustration of how shadow occlusion is formed by an obstruction in the print volume. B_1, B_2, B_n represent the subsequent projections induced into the volume. Whereas γ_1, γ_2, γ_n represent the shadow occlusion formed by the obstruction. c is the instantaneous center of the obstruction in the in-plane coordinate system and r_p, r_o, represent the radial distance of the printed part and the obstruction.

3.15 Print Time Comparison

One inherent benefits of volumetric printing is the ability for this process to produce the whole volume at once. This therefore offers some significant print time advantages over current technologies which traditionally produce parts layer-by-layer. To investigate the benefit of this technology two common additive manufacturing methods were chosen.

An Elegoo Mars DLP resin printer and an UP MINI were used for this comparison. Each printers layer height was set to 0.1 mm to ensure that the print time was comparative between the two printers. For the volumetric printing system the target geometry was reconstructed using the developed slicing software with no z-variation. A spherical geometry was chosen due to its simplicity and ease of manufacture. For each trial a sphere of radii ranging from 5 - 20 mm was printed and the print duration was recorded as per the display readout on each machine.

3.16 2D Calibration

To characterize and validate both the resin mixture and optical setup, a two-dimensional acrylic slide comprised of two sides with a 3mm air-gap was filled with the polymer mixture. The slide was then exposed to a grid pattern consisting of squares of increasing time and intensity. The aim of this was to characterize not only the time taken to initiate polymerization, but the minimum intensity required.

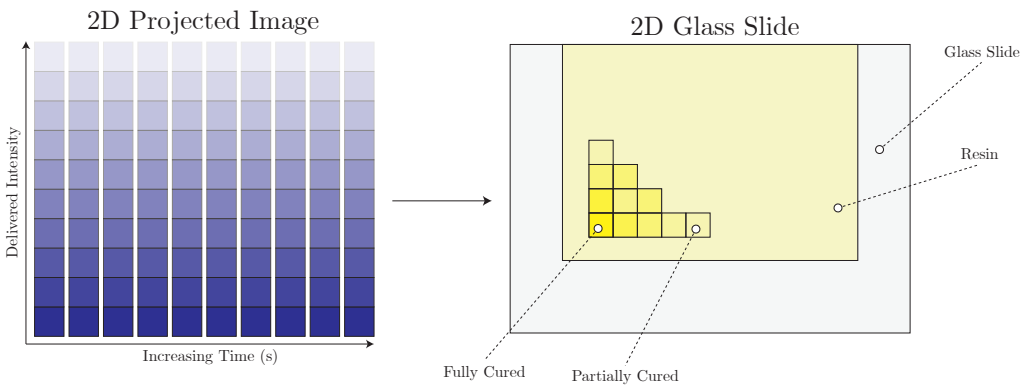

Fig. 3.17 A two-dimensional image array of varying intensity is projected into a glass slide containing the polymer mixture. This process is used to determine adequate exposure intensity and exposure time for the volumetric printing process.

3.17 3D Calibration

Though the 2D calibration does give a good insight into relative exposure times and duration, it however does not account for the through thickness attenuation of the light seen in the three-dimensional case. To achieve a more thorough intuition of this effect a series of spheres with varying intensities were projected into the pre-polymer mixture as it rotates.

Using an external camera the generation of the spheres were recorded to determine the approximate time for polymerization. Information from this study was used to inform the resin kinetics model to predict for a given intensity the approximate cure duration for a volume located at the center of the container.

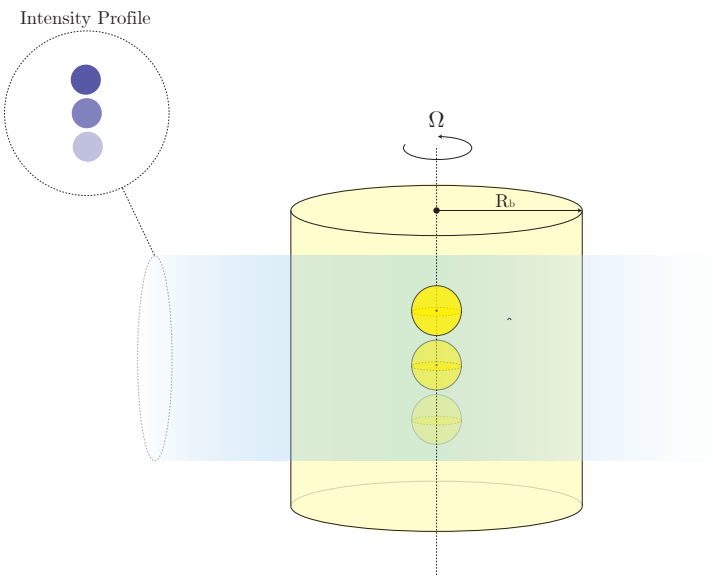

Fig. 3.18 General setup for the 3D calibration for volumetric 3D printing.

3.18 Mechanical Testing

To confirm that the use of volumetric printing does not significantly hinder the mechanical strength of the fabricated parts a series of mechanical tests were conducted on both printed and cast resin geometries. Dog-bone samples complying with ASTM D638 were cured in an acrylic mold to represent an approximate baseline of the mechanical strength of the resin system.

To complement this, a series of dog-bone samples were also printed in the build volume to highlight the effect of volumetric printing on the change in mechanical strength of the coupons. The samples were oriented such that the load direction was parelel to the wall of the build volume, as this would be traditionally the weakest part orientation in common additive processes. Each sample was post cured for an additional 90 minutes in the beam path to further improve the cross-linking of the mechanical tests. The rationale for this is to mimic the process-flow usually used in traditional stereo-lithography processes to improve the durability of printed items and to aid in producing more uniform samples between tests.

The mechanical samples were tested on an Instron 5966 load frame, with the extension and load being recorded by the load frame. The gauge cross section was calculated prior to the test to determine the average stress within the region of interest.

Chapter 4

Results

4.1 Effect of Projection Angles

The basis of the projection algorithm is built on the idea of reverse computed tomography. Because of this the accuracy of the result is highly dependent of the frequency of projection sampling. With a larger number of projections producing a more accurate reconstruction. This however, is not usually feasible due to the computational cost of producing large data sets. In most cases additional excessive projections cause a significant increase in CPU time for little impact on the reconstruction accuracy. To demonstrate this conjecture a representative slice of a test geometry was reconstructed using the developed algorithm shown in Section 2.1 for an increasing number of projections. A cross-sectional slice of the Yoda geometry was chosen, as it represents a complex topology consisting of a central volume and two satellite islands.

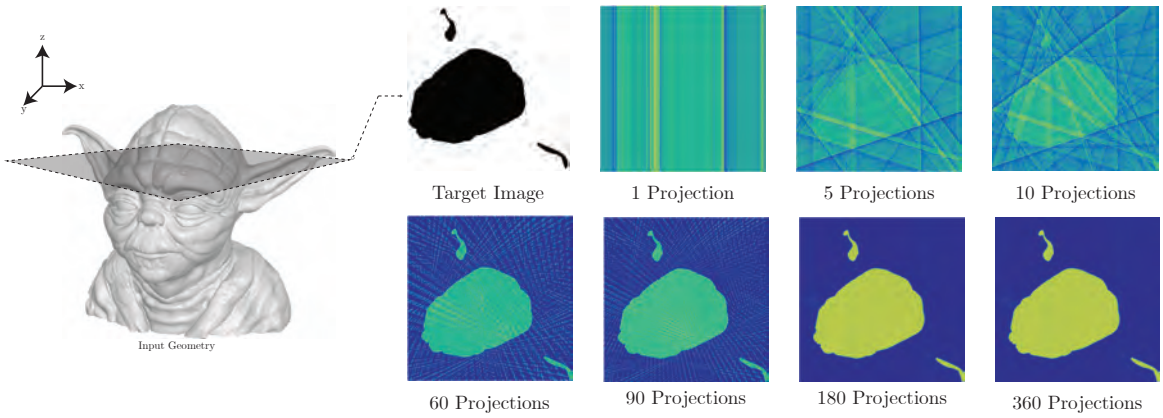

Fig. 4.1 Two-dimensional output from the projection algorithm, with incremental projection sampling.

From Fig. 4.1 we can clearly see that the an increase in the number of projection angles does to a degree improve the quality of reconstruction. However, as the frequency in which the samples are taken increases so does the computational time required to compute these cross-sections. This can more clearly be seen in Fig. 4.2 by plotting the instantaneous intersection over union for the reconstructed domain. From this we can clearly see that the accuracy is dictated by the number of projection until a point. Beyond that point, additional projections tend to have an asymptotic effect on the reconstruction accuracy.

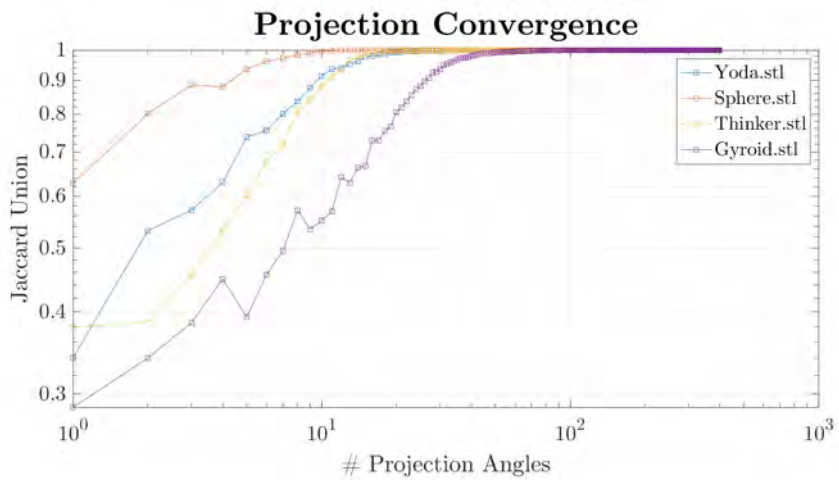

Fig. 4.2 Effect of the number of projection angles on the associated reconstruction error for various STL files.

In contrast the CPU time tends to behave linearly as shown in Fig. 4.3. Note that the plot scaling is logarithmic causing the trend to appear non-linear.

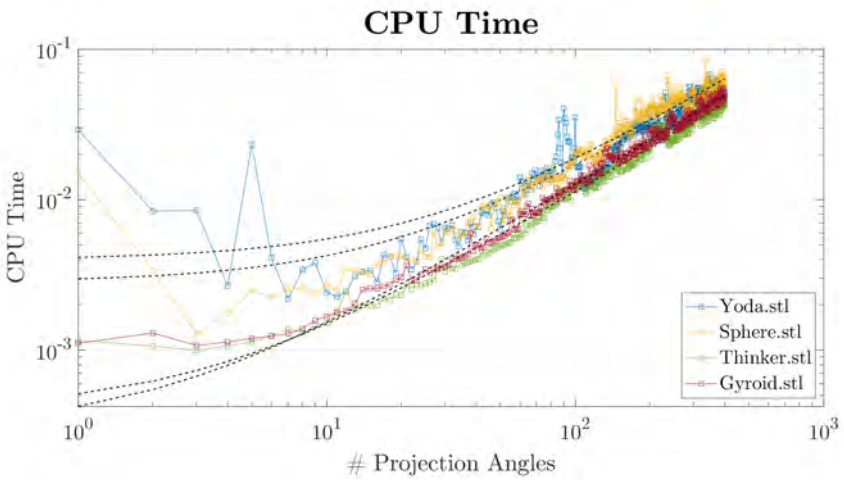

Fig. 4.3 Effect of angular frequency on CPU time.

We can therefore conclude that as expected the number of projection angles initially has a dramatic effect on the reconstruction quality, however tends to be asymptotic especially at higher projection frequencies. However, in contrast CPU time tends to be strictly linear. This therefore highlights that the number of projections should be dictated by error convergence and not by time minimization.

4.2 Tomographic Image Production

The primary goal of the tomographic projection algorithm is to determine a set of projections that when back-projected accurately represent the target geometry. This is no a trivial process, as the projections need to include the geometric representation and the robust resin kinetics model highlighted in Section 2.2. This was first tested on its ability to reconstruct simple geometries such as a cube.

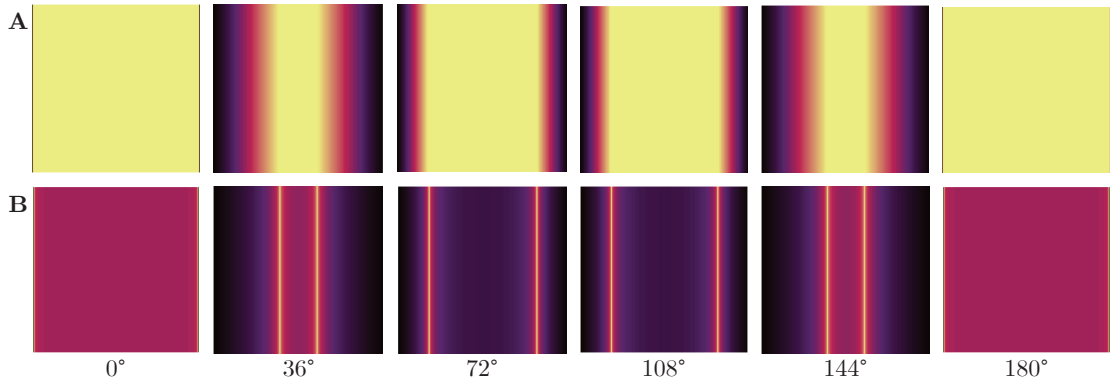

Fig. 4.4 **(A)** Un-optimized projections of cube geometry. **(B)** Optimized back projections produced by a Ram-Lak filter and positive attenuation.

As shown in Fig. 4.4 the algorithm is able to accurately determine the unfiltered cross-projections of the cube model effectively. However, as highlighted in previous sections this output will not accurately recreate the target geometry due to high spacial projections causing over exposed regions of the target geometry. To combat this, iterative filtering techniques are applied in the Fourier domain such that these projections only ensure critical curing of the volume.

To validate the ability of the approach to extend to more complex geometries, the Yoda test model highlighted in Section 2.1 was used. This model contains a complex surface topology and thin features that are difficult to accurately reconstruct due to the under-representation of the radon transform in these regions.

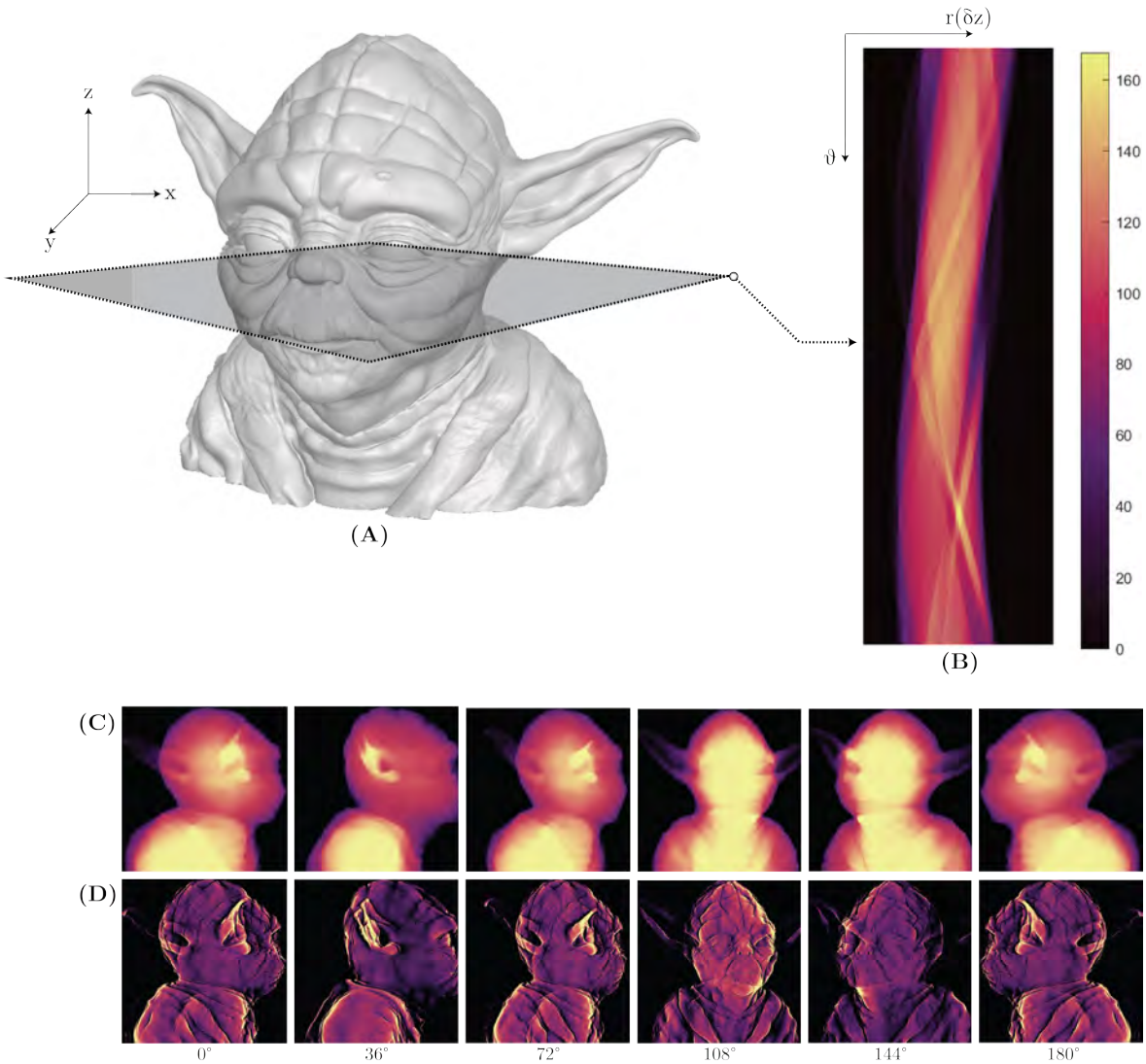

Fig. 4.5 **(A)**Input STL file of Yoda geometry. **(B)** Sinogram representation of the 2D radon transform applied to a single slice. **(C)** Un-optimized projections of a yoda target geometry from sequential stacking of the radon transforms. **(D)** Optimized back projections produced by a Ram-Lak filter and positive attenuation.

As shown in Fig. 4.5 unfiltered projections still do produce unfavorable results often resulting in blurry images due to the over representation of low frequency noise in the images. However, in contrast filtered projections are able to not only clearly capture the target geometry but increase projection intensity in under represented regions of the target volume. This is extremely important to ensure accurate reconstruction of fine details. As these regions tend to be under represented by the radon transform. This can be clearly shown in the ears of the Yoda model shown in Fig. 4.5.

4.3 Tomographic Reconstruction

Section 4.2 was able to illustrate the ability for the reconstruction algorithm to produce a set of high quality projection images. However, without validation that these images are capable of reconstructing the target geometry they are meaningless. This section aims to demonstrate the validity of these projections by accurately reconstructing a mesh solely based on the projection set. In addition we would also like to demonstrate that the saturation of projections highlighted in Section 4.1 also extends to three-dimensions.

The goal of the projection algorithm is to determine a set of projections that only critically cure each voxel of the input geometry in the output space. As highlighted in previous sections, filtering of these projections is imperative to guaranteeing this constraint without over curing. The first part of Fig. 4.6 demonstrates the effect of unfiltered projections which causes exponential over curing, leading to a fully cured volume. However, in contrast filtered projections are able to accurately represent the model. This is because each image is linked and optimized to the subsequent projections. Furthermore, as seen in Section 4.1 the accuracy of the the model is dictated by the frequency of projections, with an increasing number of projects resulting in a higher intersection over union of the parent model.

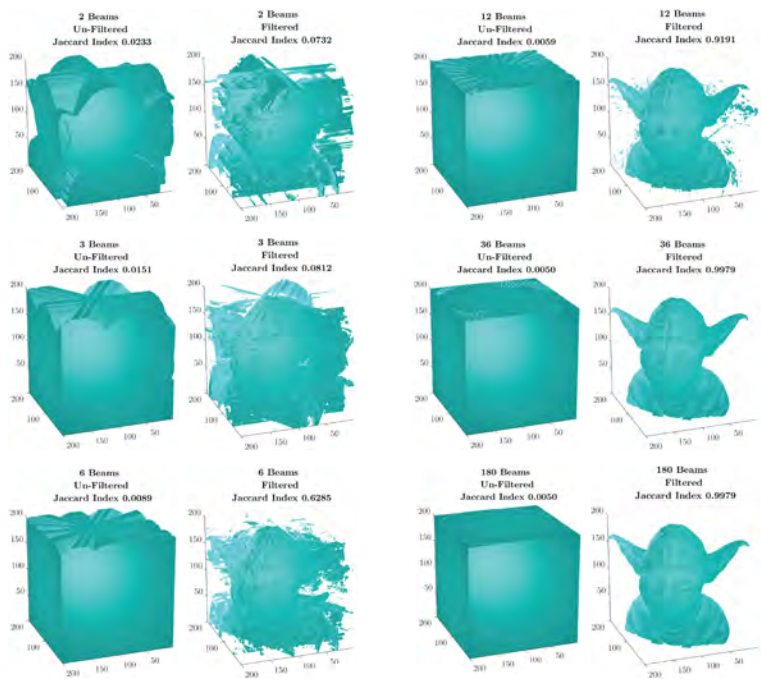

Fig. 4.6 Virtual reconstruction of the Yoda test geometry, highlighting the comparison between the filtered and unfiltered output.

In addition to complex external cavities such as the ones shown on the yoda model, the algorithm is also capable of correctly reconstructing intricate internal cavities and small features. To illustrate this, a gyroid was chosen as it represents complex internal cavities, in addition to a cubic lattice highlighting the capacity to replicate small features Figure 4.7.

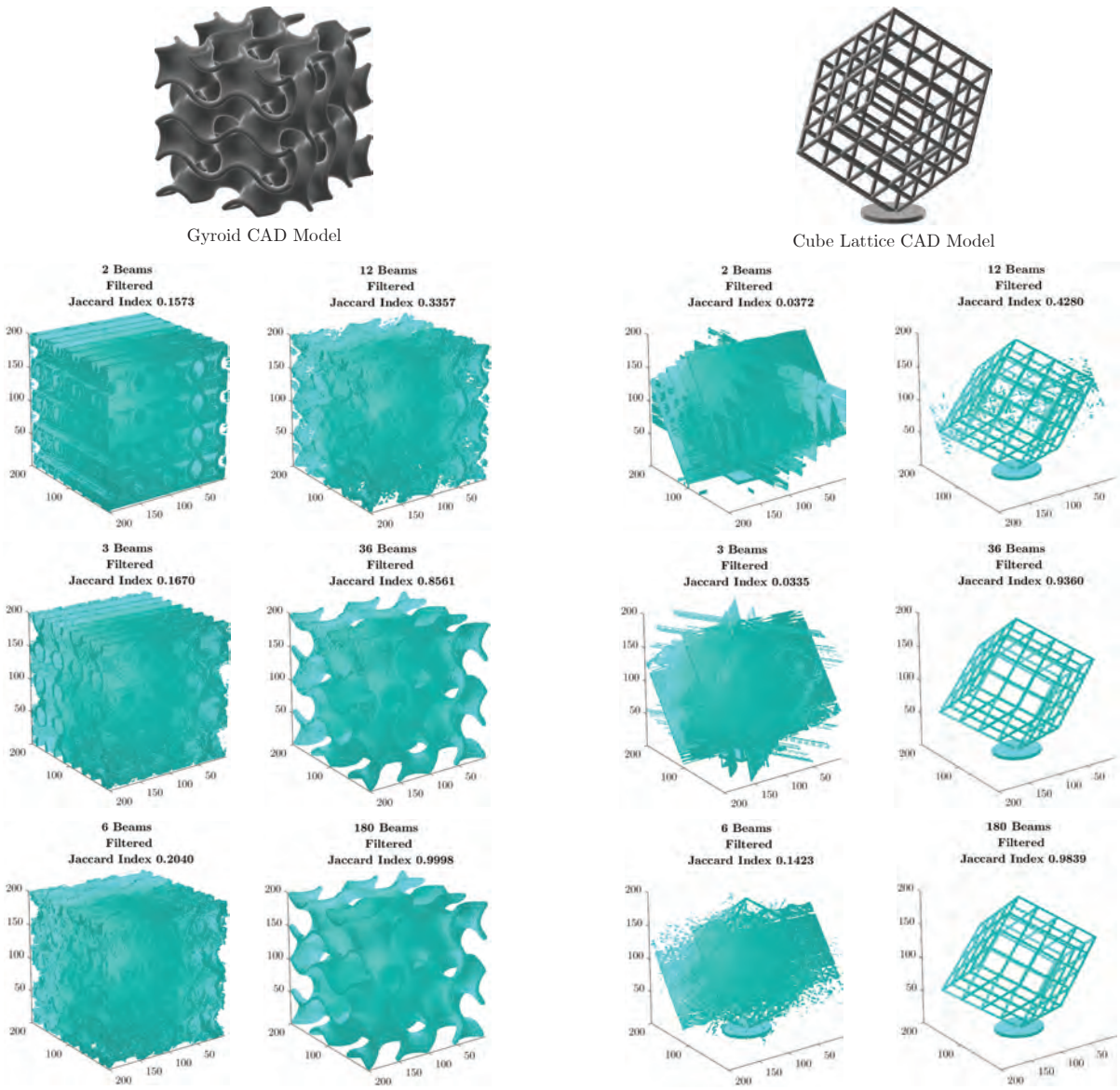

Fig. 4.7 Virtual reconstruction of the Yoda test geometry, highlighting the comparison between the filtered and unfiltered output.

To properly explore the effect that an increasing number of projections has on the convergence of the model, the jaccard index has been plotted for a small subset of geometries Fig. 4.8. As shown, we can see that the convergence of the model is not identical for each geometry, with more complex geometries often requiring greater number of projection to converge to the target. This is most likely due to the reduction in intensity for fine regions due to the through thickness radon transform being lower in these cases. As the curing is not linearly dependent on the intensity, small variation in the magnitude of the projection can cause significant reduction in the effectiveness of the image.

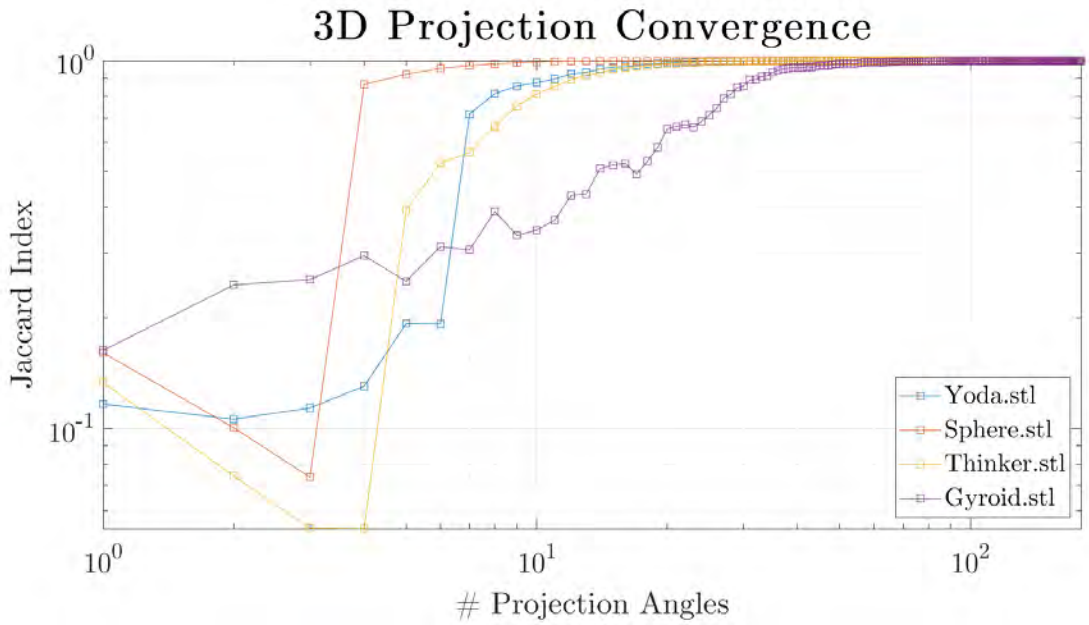

Fig. 4.8 Plot of the convergence of various input geometries as a function of the number of projection angles.

The implication of non-linear curing will cause issues in geometries that contain both high and low cross-sectional areas. As the radon transform is loosely related to the cross-sectional area of the part, regions with low areas will attract reduced intensities. This may prove difficult to simultaneously cure the volume due to the curing rate being exponentially related to the intensity. Additional thresholding steps will be required to achieve concurrent solidification.

4.4 3D Curing Engine

The 3D curing engine was developed to aid in predicting the cure duration, in addition to visualizing how the part begins to cure over time. This process works by relating the energy delivered and held within each voxel for a given time period and the kinetic equations outlined in Section 3.2 and Section 3.5. The outcome of this process is the ability to gain insight into the development of the geometry that would be impossible to observe during printing. The engine is able to predict an approximate print duration and highlight the solidification development under a rotating print volume.

The engine was validated on a subset of complex geometries to observe how curing takes place within the volume. Figure 4.9 shows the progression of the eiffel tower over a period of 0 - 60s. Fig. 4.10 demonstrates the advancement of the yoda test geometry over a period of 0 - 43s.

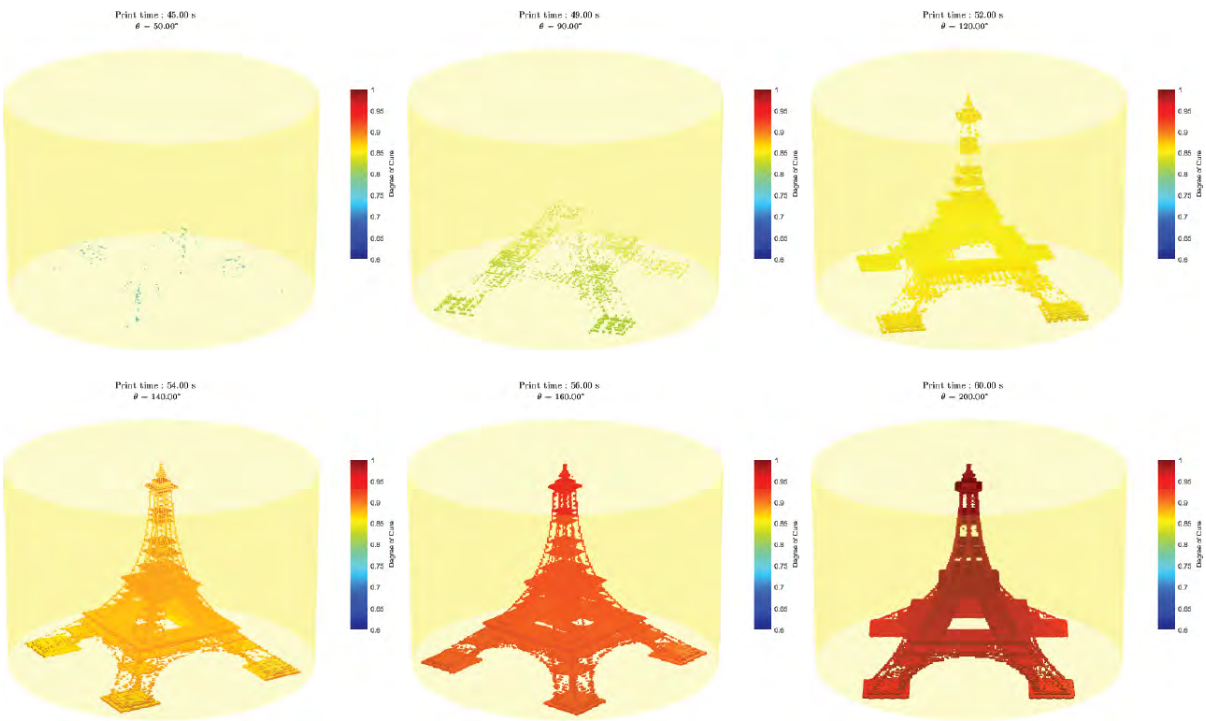

Fig. 4.9 Kinetic simulation of the development of the eiffel tower geometry for a time period between 0 - 60s. The colour scale represents the degree of cure of the part within the volume throughout the print period.

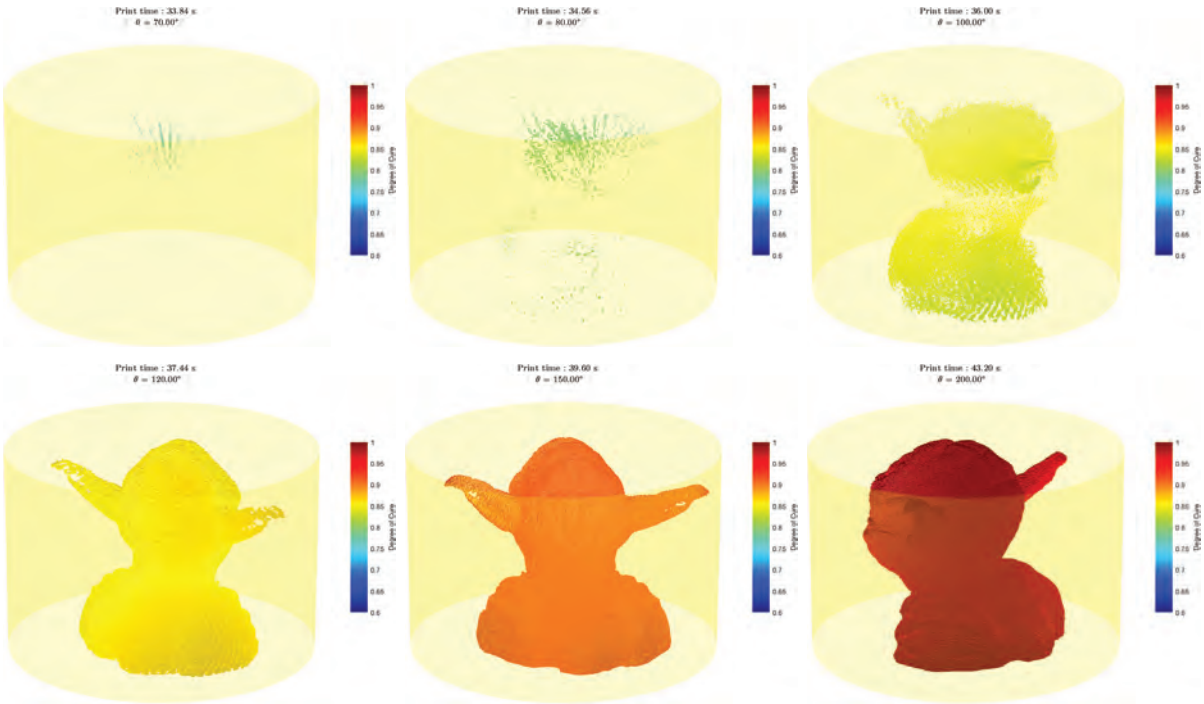

Fig. 4.10 Kinetic simulation of the development of the yoda geometry for a time period between 0 - 43s.

From the kinetic simulation we can observe that both the curing rate and progression is non-uniform throughout the volume. This therefore causes significant implications in accurately predicting the print time and ensuring that all voxels are critically cured. However, these spacial time dependent discrepancies does allude to the possibility of implementing a projection optimization procedure to guarantee simultaneous solidification. To improve the accuracy further, oxygen inhibition will need to be added to the kinetics model. As this effect greatly impacts the duration of exposure prior to the onset of curing.

4.5 Volumetric Slicer

To facilitate the ability for this new technology to be used by a wider range of audiences, a rudimentary volumetric slicing package was developed within the MATLAB environment that incorporates all of the aforementioned slicing, resin kinetics and projection algorithms into one single package Fig 4.11 .

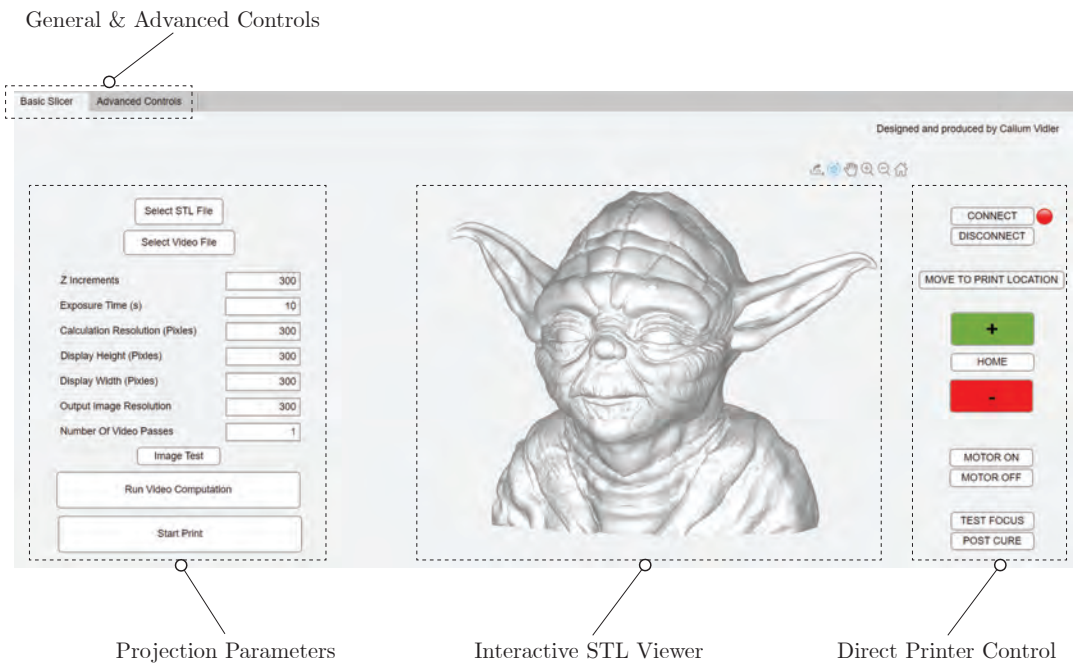

Fig. 4.11 Various sections of the volumetric slicing software and how they relate to the operation of the printer

The left most side of the graphical user interface (GUI) involves the ability to select an input STL file to be sliced, or an already sliced video file to be played for printing. In addition to parameters that effect the output video file, and projection parameters. Additional advanced controls can also be found which enable users to precisely control the output produced by the slicer, as well as input custom reconstruction parameters depending on their use case. The slicer also includes a basic mesh plotter to inspect the input STL prior to printing, which includes the ability to move, rotate and scale the STL as required.

The right hand side of the GUI is for printer control. Though the process of printing is completely automated, with the volume being inserted and removed by the beam path without user interaction, some additional controls are also available. These controls are primarily used for print calibration and alignment of the printer.

4.6 Mechanical Design

For this project, two separate mechanical systems were developed to investigate and determine the benefits and limitations of this technology. Initially, a prototype system was developed to determine a proof of concept of this technology as the idea and concept was in its infancy. The second portion of the project was spent developing a new mechanical system that hoped to correct some of the underlying issues with the initial system.

4.6.1 Mechanical Design: Version 1

The following figure, Fig. 4.12 represents the first initial prototype of the volumetric printing system. The system leverages the use of a standard desktop projector and vertical gantry for micro-alignment of the polymer container with the beam path. The positioning and control of the system is achieved through a control box located on the rear of the machine, which interfaces with the slicing software shown in previous sections.

Though this system enabled rudimentary reconstruction of simple geometries, it was unfortunately extremely limited due to the illumination system. Though the desktop projector provided a simple approach to this problem, the optics did not provide an adequate beam collimation which is imperative for accurate reconstruction. To correct for this, a new system was designed that hoped to enable both greater optical power and beam alignment.

Fig. 4.12 Prototype volumetric printer highlighting the various components.

4.6.2 Mechanical Design: Version 2

The second version of the volumetric printing system was developed with hopes of improving the overall print accuracy and dose delivery system to the volume. Fig. 4.13 depicts the layout and design of the mechanical assembly. This approach relied on the use of a high powered 445nm laser coupled with a transparent LCD display for beam masking. The primary focus of this approach was to negate the irregularities in both the beam collimation and gaussian image profile of the version 1 printer.

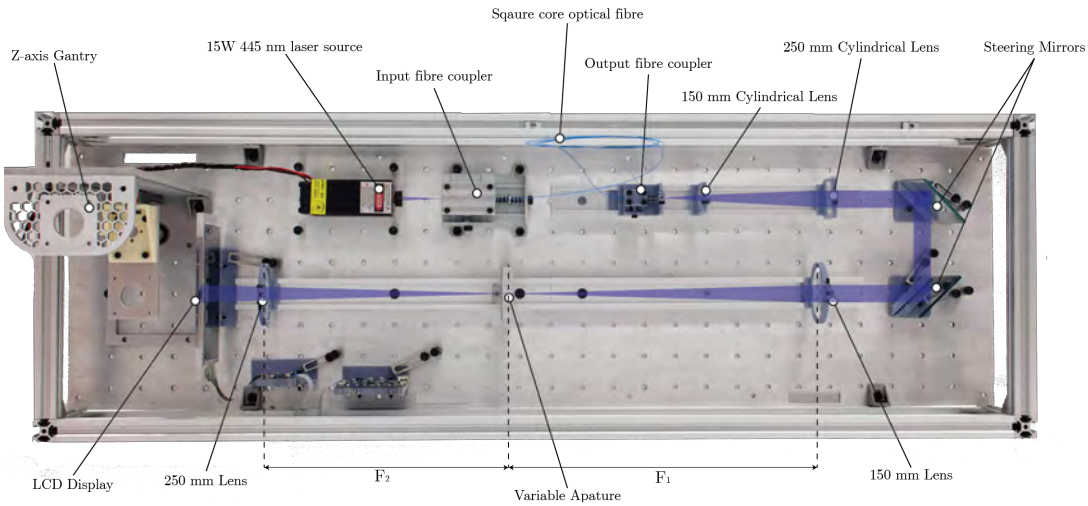

Fig. 4.13 Second revision of the volumetric printing system highlighting the components and approximate layout within the chassis.

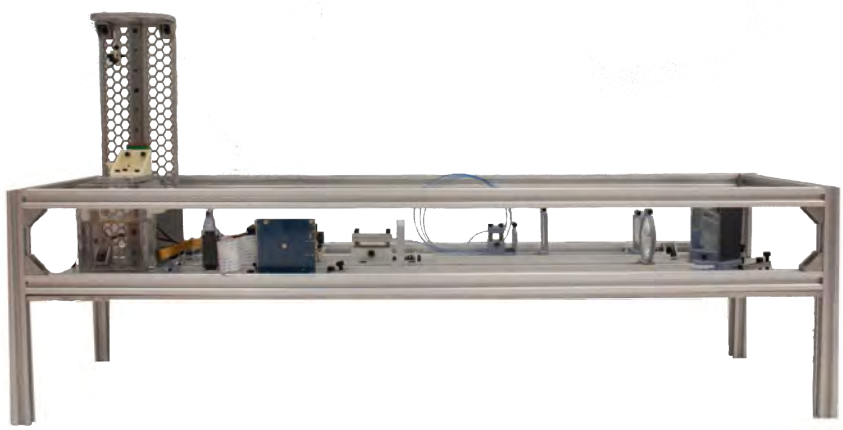

Fig. 4.14 Second revision of the volumetric printing system from the side view of the assembly

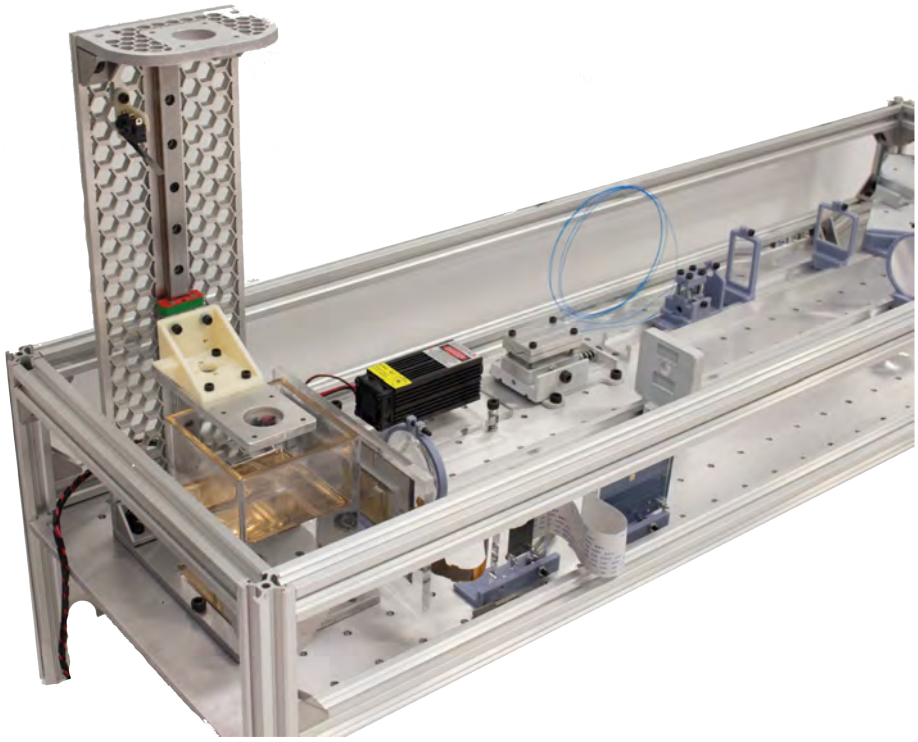

Fig. 4.15 Second revision of the volumetric printing.

The current state of the MK2 printer has developed a lot of the preliminary ground work and mechanical system. However, due to budget constraints with the project the system had to move away from the initially propsed DLP setup and towards a more cost effective LCD display. This change has significant implications of the output image due to the large amount of dispersion and attenuation caused by the transmissive display. This caused two primary issues. First a large amount of energy was required to ensure a minimum amount of light was present in the far field. However, the large amounts of energy absorbed by the display due to the poor optical efficiency caused significant thermal runaway and in turn optical instabilities. Secondly, the image formed by the display was extremely un-collimated due to diffraction caused by the polarizing films and internal liquid crystals, making the image un-usable in the far field.

Due to the inability to produce a good image with this device, further development of the assembly was halted and the MK1 printer was used for the remainder of the testing. Despite the failure of this approach, the theoretical basis still holds true for using this technique with DLP technology.

4.7 Resin Development

The polymer developed for this project is an integral part in the success and development of the volumetric printing system. Unlike traditional SLA/DLP resin systems the polymer developed for this project needed to be both highly viscous and blue light reactive. Initially, the high viscosity polymer was developed with a photo-initiator phenylbis(2,4,6-trimethylbenzoyl)phosphine oxide also known as Igracure 819, due to its availability and extensive use in dental applications.

As shown in Fig. 4.16 we can clearly see that Igracure 819 is primarily absorbent in the ultra-violet range with a small window of absorbance in the visible blue spectrum ($\approx$ 445nm). Though this photo-initiator did provide some indication of reactivity to blue light, parts produced using this photo-initiator lacked structural integrity and were often poorly reconstructed due to the low absorbance.

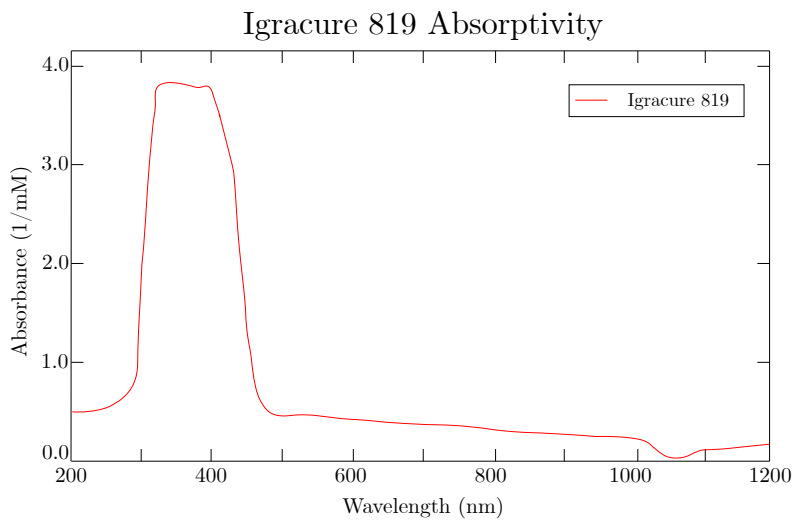

Fig. 4.16 Result of ultraviolet–visible spectroscopy on photo-initiator Igracure 819.

For the majority of the work conducted in this project a new resin system was developed to ensure greater reactivity on incidence to blue light. The polymer combination remained the same to the previous resin, however Camphorquinone with co-initiator Ethyl 4-(dimethylamino)benzoate was added to enable blue light curing.

Ultra-violet visible spectroscopy shown in Fig. 4.18 illustrates a significantly higher incidence absorbance in the blue spectrum compared to that of Igracure 819. Which highlights the ability for this resin to be orders of magnitude better in the visible range to that of Igracure 819.

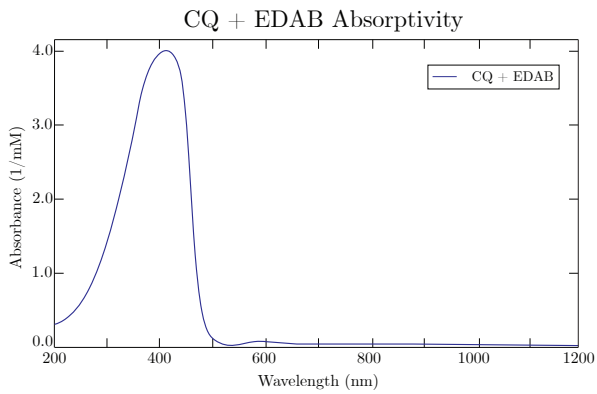

Fig. 4.17 Result of ultraviolet–visible spectroscopy on photo-initiator CQ

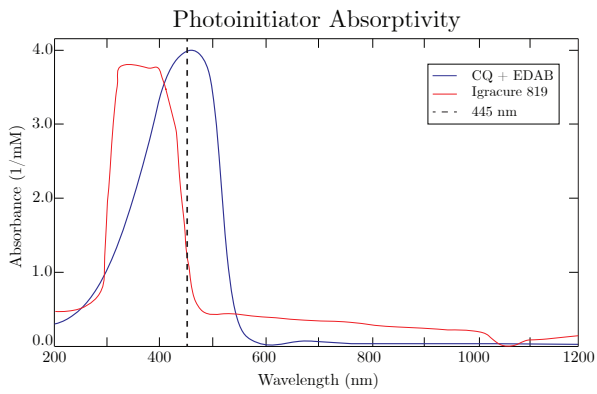

Fig. 4.18 Comparison of the two developed resin systems at 445nm.

The ability for this resin system to absorb blue lights is highly evident when observing the pre-polymer mixture containing the photo-initiator Fig. 4.19. On inspection we can see that the resin has a translucent yellow tint, which indicates the high absorption of light in the blue spectrum.

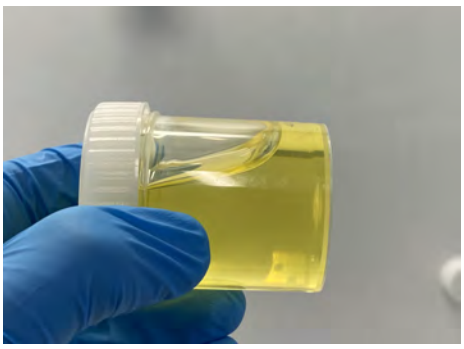

Fig. 4.19 Image highlighting the color of the developed monomer resin. The resin exhibits a yellow tint due to the high blue light absorbance. Furthermore, you can intuitively see how viscous the resin is by the meniscus formed.

4.8 Two-dimensional Calibration

To characterize the effect of the algorithms ability to represent two-dimensional images, a projection map containing varying intensity and cure profiles was evaluated. With the purpose of this test to explore the minimum intensity and cure duration required for solidification.

As shown in Fig. 4.20 we can clearly see that the degree of cure is dependent on the delivered dose and not duration or intensity independently. We can thus build a solidification gradient that represents the total possible set of variant combinations required to solidify the volume.

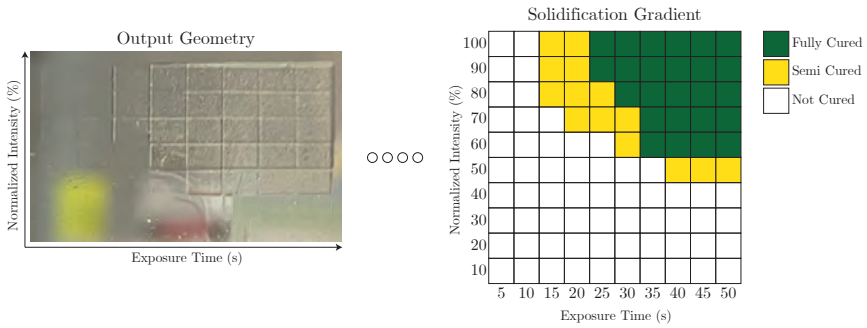

Fig. 4.20 Degree of cure map for two-dimensional printing

The following set of images show the ability for the reconstruction algorithm to categorize more complex topologies consisting of voids and sharp edges. As shown in Fig. 4.21 the dense reconstruction of the 2D image is able to accurately construct a sharp and highly defined image in both cases in a matter of seconds.

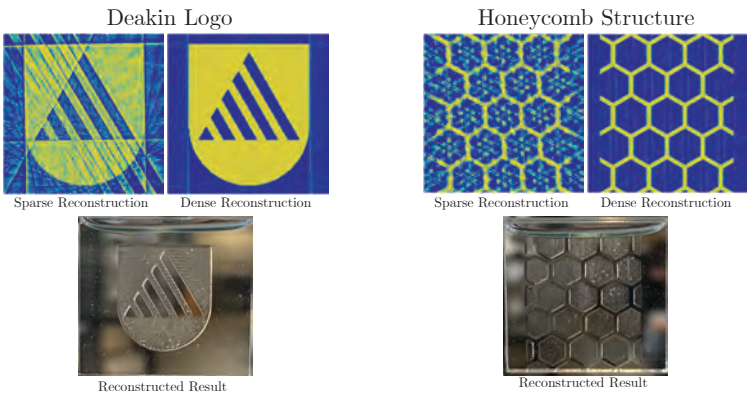

Fig. 4.21 The required projection image was first iterated until convergence and projected into the volume. (Left) Deakin logo reconstruction and projection. (Right) honeycomb pattern reconstruction and projection.

4.9 Three-dimensional Calibration

To characterize the effect of beam intensity in three-dimensions, the rotating volume was subjected to an decreasing intensity of spheres. The image below, Fig. 4.22 illustrates the development of the volume as a function of time.

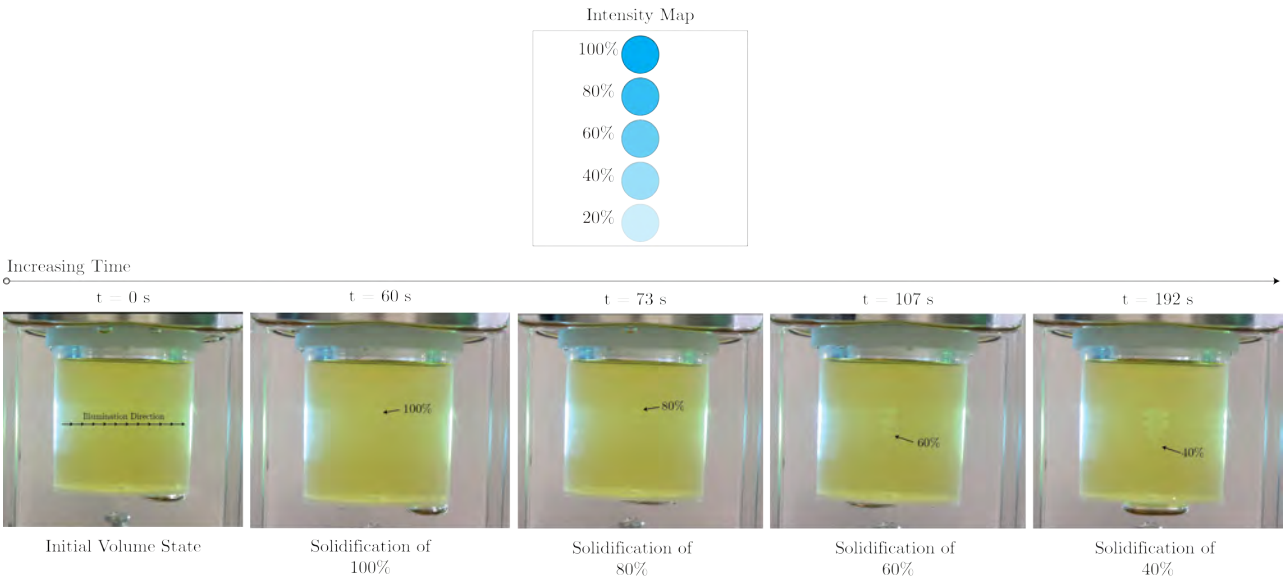

Fig. 4.22 Effect of the beam intensity of solidification rate of the pre-polymer mixture. Illumination is from left to right of the volume, with the incoming arrangement being approximately that of the intensity map. Note, the image of the 20 % cure duration is not shown in this figure.

As expected the rate of cure of the pre-polymer mixture is highly dependent on the intensity as well as the duration of cure. This can more clearly be seen by plotting the projection intensity as a function of the normalized time. Where the normalized time represents the subsequent projection time divided by the time to cure for full intensity. As shown in Fig. 4.23 the solidification time increases exponentially with the reduction in input intensity.

For intensities lower than 20% these areas typically become attenuated and diffused by the polymer-mixture and as a result have no impact on the final geometry. Therefore, this confirms the hypothesis that projections below a critical threshold need to be truncated to ensure that locations with low cross-sections are correctly represented by the algorithm.

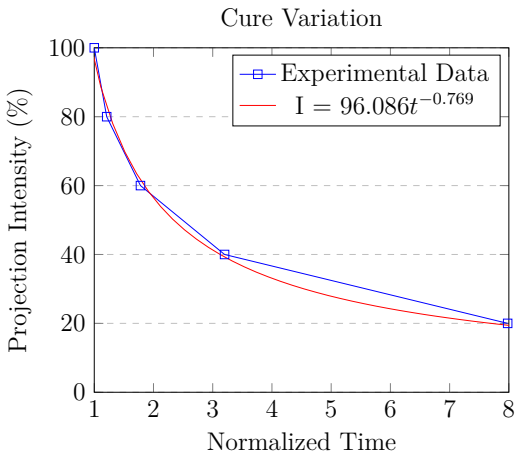

Fig. 4.23 Normalized time to cure for varying intensity functions

4.10 Printing of a Sphere

Now that the system has an intuitive understanding of how intensity and time effect the outcome of printed objects, a larger object was printed to test the ability to reconstruct simple geometries. Fig 4.24 shows a time-lapse illustration of the development of the sphere geometry over time. As shown, the geometry was reconstructed in-situ in approximately 35 s without the need of supporting material.The generated geometry is shown to be optically smooth and absent of any layer lines due to the geometry being created via a cumulative dose of light.

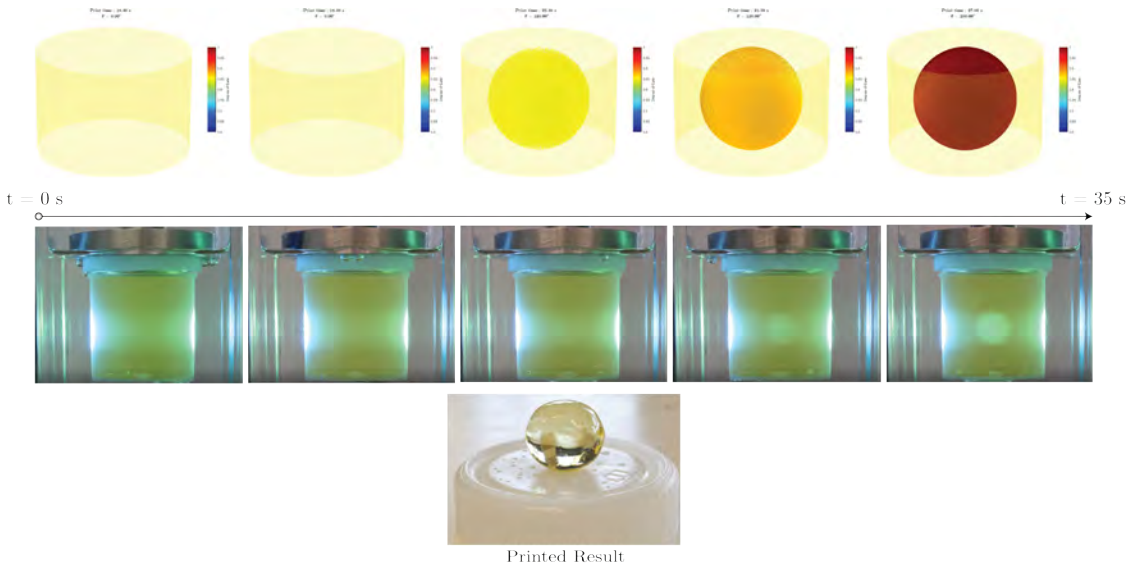

Fig. 4.24 Volumetric printing of a spherical geometry.

4.11 Printing of a Cylinder

A cylinder was printed to characterize the collimation of the image produced by the printing system. Images with an adaquate amount of beam colimation will produce a cylinder with two parallel faces. Fig. 4.25 illustrates the development of the cylinder over a 38s period in addition to the printed result of the cylinder.

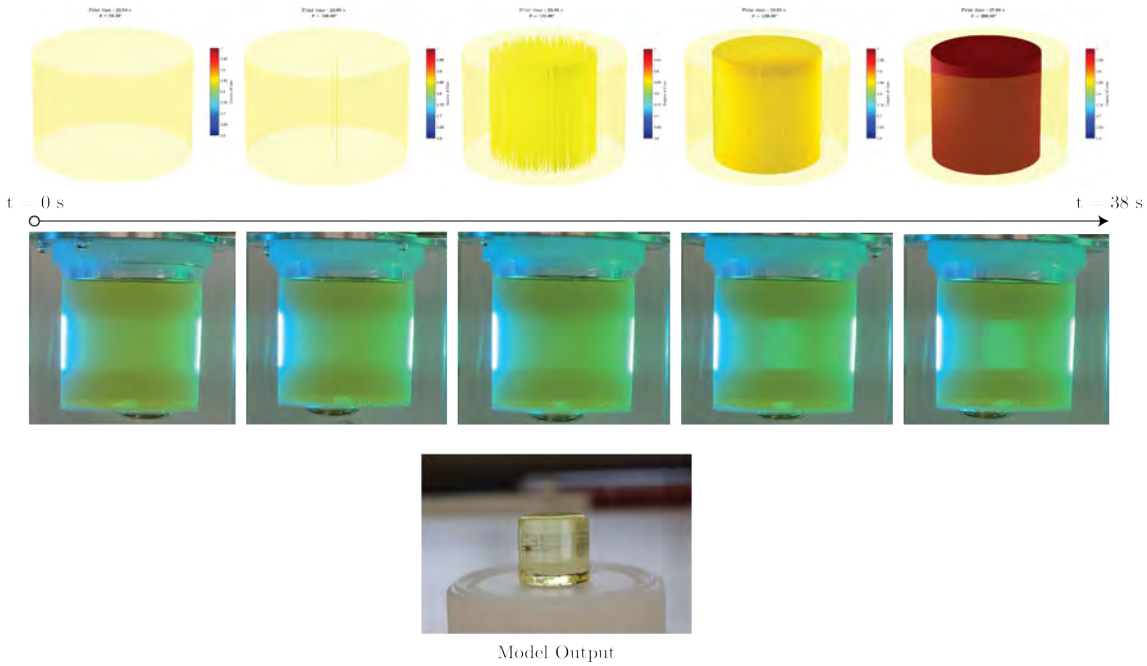

Fig. 4.25 Volumetric printing of cylindrical geometry.

As shown, the cylinder exhibits good parallelity between the upper and lower faces indicating the presence of a high degree of beam collimation. Furthermore, the printed result is bereft of layer striations which result in an optically smooth surface finish.

4.12 Printing of a Martini Glass

The hope of this technology is to one-day be used in a similar fashion to the Replicator from star-trek in where Picard was able to materialize a martini glass from thin air. As a tribute to this vision, a martini glass was chosen to illustrate the ability for the printer to replicate this.

The martini glass offers somewhat of a challenge to print, due to it having a non-constant radial cross-section and thus is highly dependent on the transverse threshold applied to the projection image highlighted in Section 3.3. Furthermore, the hollow section at the mouth of the cup tests the ability for the printer to reconstruct thin hollow regions of material. A transverse thresholding of 45% was applied in this scenario to ensure instantaneous solidification.

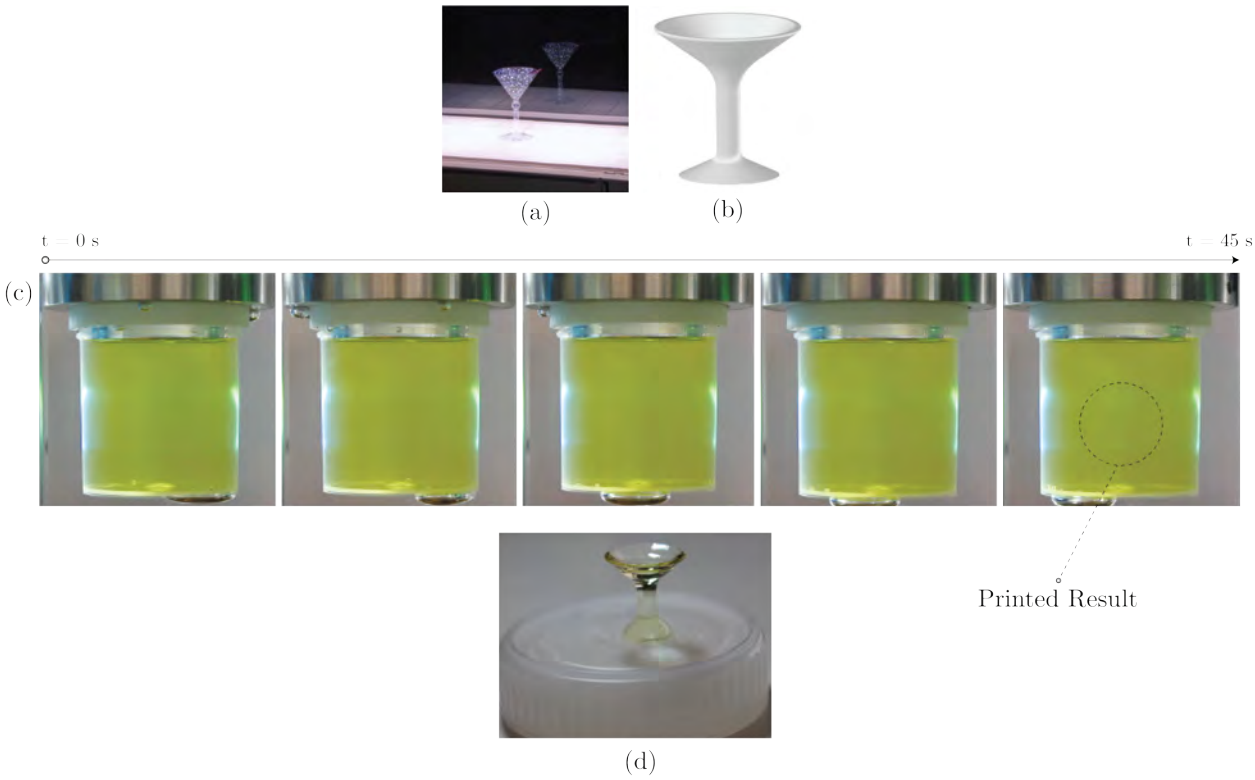

Fig. 4.26 Volumetric printing of a martini glass. (a) Star-trek replicator (b) Input STL file (c) Development of the martini glass over a period of 45 seconds. Note it is difficult to distinguish the printed geometry as the refractive index of the cured media is similar to that of the uncured media. (d) Printed result of the martini geometry.

As shown in fig. 4.26 the volumetric system was able to accurately reconstruct the target geometry with a high degree of accuracy in approximately 45 seconds.

4.13 Volumetric Overprinting

One of the interesting implications of this technology, is the ability to form geometry around already existing structures. This technique is not possible with any currently available additive manufacturing methods today and is analogous to over-molding techniques commonly used in manufacturing. To explore this technique a metallic rod was suspended within the center of the volume as shown in Fig. 4.27 and an example of a handle was printed over the metallic structure.

As the rod creates optical occlusion present in the volume due to the obstruction, the over-printing algorithm shown in Section 3.14 was used to preserve geometry in shadowed regions. As shown, the algorithm was able to reconstruct the input geometry to a high degree of fidelity, despite the fact that in most cases only half of the geometry could be exposed due to the obstruction.

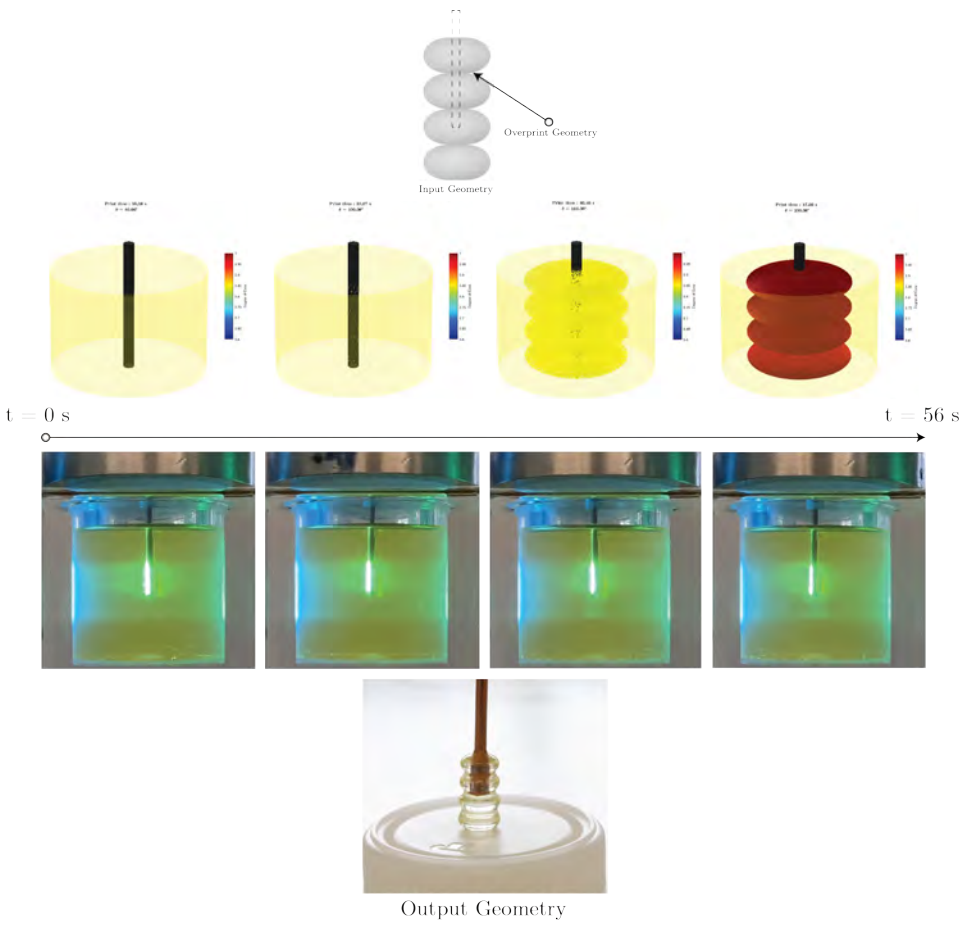

Fig. 4.27 Printing of a handle like geometry onto a fixed metallic rod. This process is analogous to traditional over-molding techniques such as the handle of a screw driver.

4.14 Printing of a Simple Lens

Producing optically clear parts with traditional AM has always been a challenge due to the occurrence of layers producing unwanted diffraction patterns. One of the interesting implications of volumetric printing is the ability to produce objects that are optically clear and without traditional layer lines. This new approach to manufacture opens up a wide range of possible uses for objects that rely on optical clarity, such as the ability to rapidly manufacture low cost lenses in a matter of seconds.

Fig. 4.28 demonstrates the capability for a volumetric printing system to rapidly produce simple lenses in-situ that is capable of magnifying text. Though this is only a proof of concept, it does however illustrate the possibility for this technology to be applied to optics due to its superior optical clarity over traditional addative manufacturing technologies.

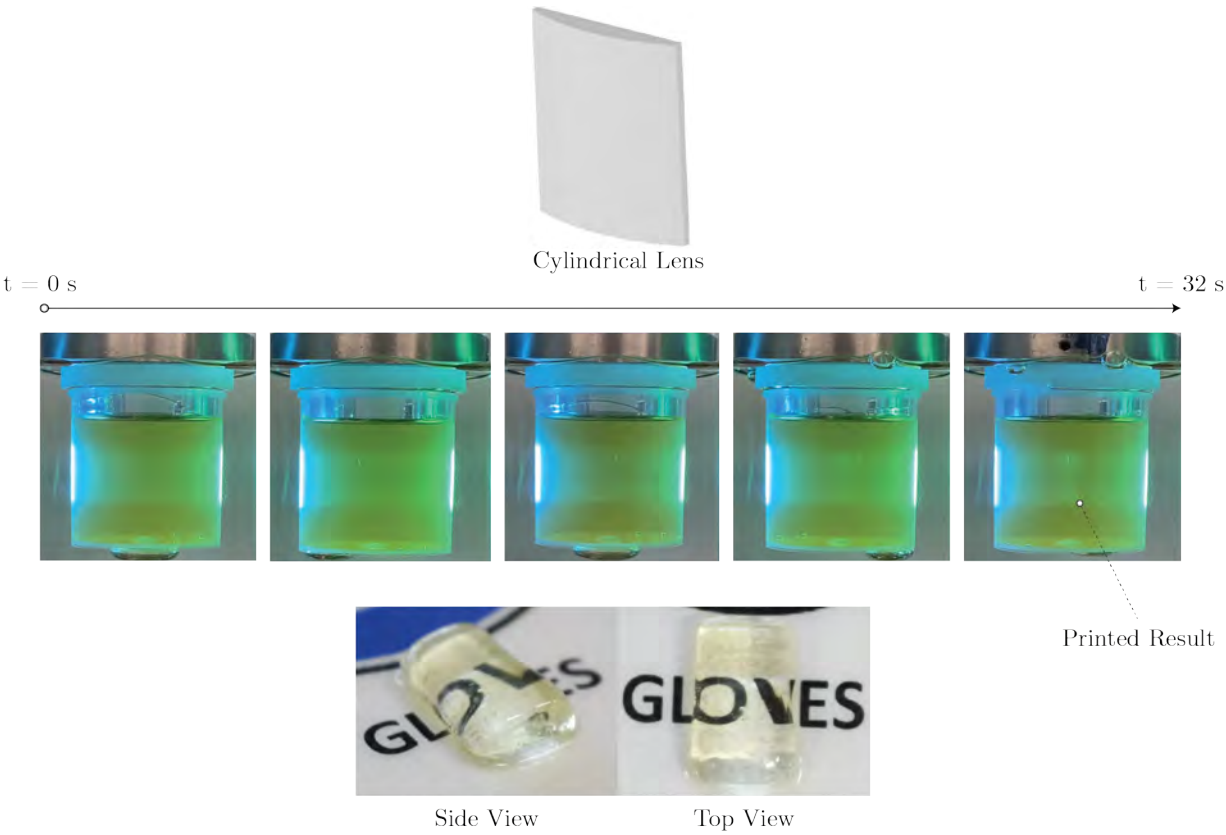

Fig. 4.28 Rapid manufacture of a simple cylindrical lens.

4.15 Comparison of Print Times

One of the undeniable benefits of volumetric printing is its ability to fabricate geometry extremely quickly, due to instantaneous solidification of the target geometry. However, was is not directly clear is if this rapid manufacture is independent of the size of the object. To investigate this, geometries of varying size were volumetrically printed (VP) and compared against common AM methods. The following set of results represent the comparison of these print times for FDM, DLP and VP.

Geometry Size	Volumetric (s)	FDM (s)	DLP (s)
5 mm	32	165	918
10 mm	35	416	79
15 mm	42	706	2250
20 mm	47	1089	2946

Table 4.1 Results for the investigation of print times for common additive manufacturing methods.

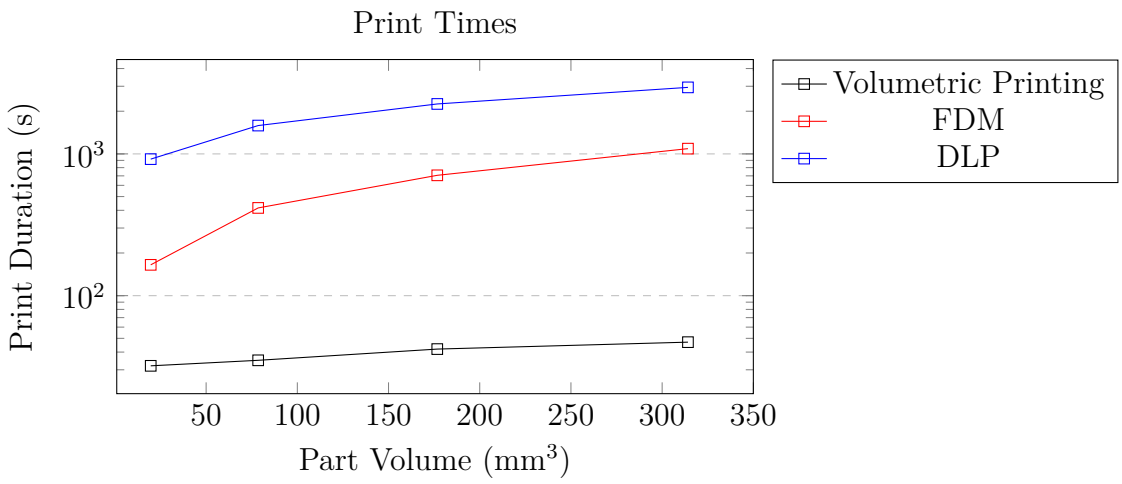

Fig. 4.29 Comparison of print times for common additive manufacturing methods.

As shown in Fig. 4.29 volumetric printing tends to be orders of magnitude faster than common currently available technologies. Where in some cases part production via volumetric printing is 60 times faster than DLP. Furthermore, unlike traditional manufacturing methods, volumetric printing does not have a significant variation in print time for a increase in part volume. This illustrates a significant paradigm shift in manufacturing as traditionally part creation time is highly dictated by the size of the object that you wish to make.

4.16 Mechanical Characterization

Traditionally additively manufactured parts tend to behave anisotropically due to the layering nature of their manufacture. This tends to be challenging for engineering applications as it requires precise orientation of the part prior to printing. However, in contrast producing the part simultaneously and bereft of layering tends to negate these issues. To explore this, a baseline result of the polymer was conducted by casting the material in a mold. This is to represent the theoretical maximum strength of the part prior to printing. As shown in Fig. 4.30 we can expect a maximum strength of approximately 35 MPa for the cast sample.

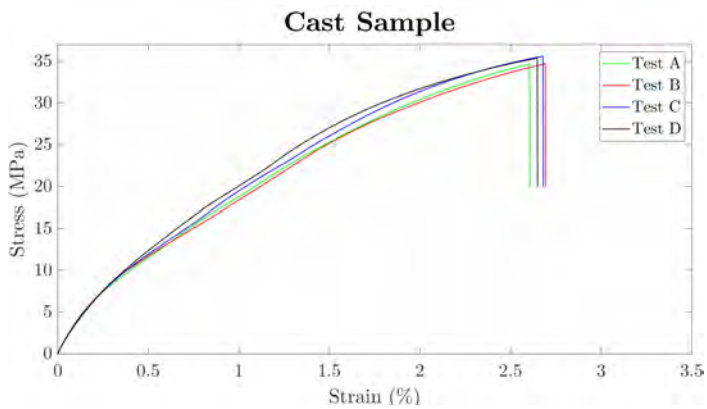

Fig. 4.30 Mechanical strength of cast photo-polymer resin.

To investigate whether parts printed via a volumetric method behave isotropically, a series of representative dog bone samples were also printed within the volume, with the direction of the sample parallel to the wall of the volume as shown in Fig. 4.31

Fig. 4.31 Volumetric manufacture of the dog-bone sample in-situ. Print time was approximately 51 seconds.

The following set of results shown in Fig. 4.32 highlight the mechanical strength of the volumetric printed dog-bone for a series of 4 samples.

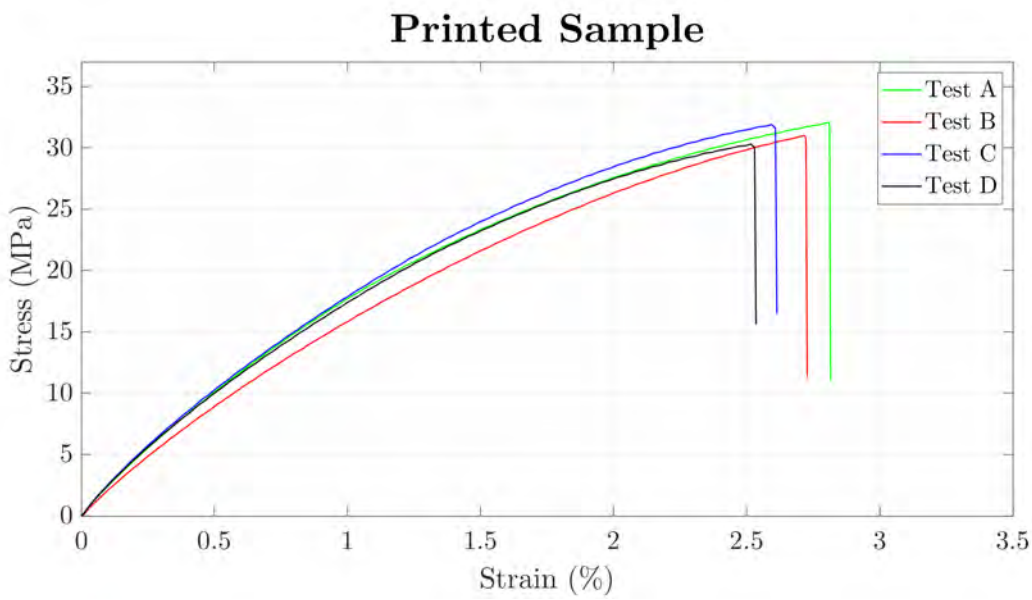

Fig. 4.32 Mechanical strength of the volumetric printed dog-bone sample.

As shown, we can see that the mechanical strength of the volumetric printed dog-bone is similar to that of the cast sample, with only a slight reduction in the mechanical strength of the part. The part was printed in the vertical orientation as this traditionally would be the weakest orientation for common AM parts. The reduction in mechanical strength could be due to the oxygen diffusion at the boundaries of the sample leading to irregularities in the cross-sectional area of the specimen. Moreover, oxygen inhibition at the walls of the specimen prevent complete curing of the polymer which may have led to this effect which is not present in the cast samples due to mold being airtight. Further investigations may need to be conducted in low oxygen environments to determine if this is a factor in the final mechanical strength of the parts.

With that being said, volumetric printed parts seem to behave isotropically resulting in near similar mechanical strength to pristine samples. This therefore, highlights a significant advantage of this approach over traditional layer-by-layer additive processes, with the potential for this technology to be more applicable to engineering applications due to the increased predictability of this process.

Chapter 5

Discussion/Future Work

The present work has demonstrated a new paradigm shift to the way in which parts can be manufactured, enabling semi-complex geometries to be fabricated in a matter of seconds. This approach hopes to foster a shift away from traditional layer-by-layer additive manufacturing and towards a method that is designed to consider the whole volume at once. This approach has been demonstrated to have significant implications, specifically in regards to the inherent flaws of traditional additive manufacturing technologies such print speed and surface quality.

The present work has demonstrated nominal print speeds in the order of 30 - 120 s, which in most cases is orders of magnitude quicker than any available technology today. Furthermore, the optical clarity of these printed parts is similar to that of cast geometries due to the unique manufacturing process that prevents the formation of traditional layers. Additionally, it has been shown that parts generated via volumetric printing exhibit isotropic behavior which greatly expands the opportunity for this approach to be applied to engineering applications. Finally, the ability for this process to print geometry in/or around already existing parts is a concept completely new to additive manufacturing and has the potential to enable fully assembled parts to be made in-situ.

The current state of the project has also developed two functional volumetric prototypes that highlight both a low-level approach via the use of commonly available projection systems, in addition to a high level approach that hopes to edge on improving the overall print accuracy and decreasing print time. Furthermore, a new slicing algorithm has been developed that is capable of taking any arbitrary geometry and representing it as a set of integral projections, that include low-level resin kinetic

understanding in addition to a simulation engine for predicting the development of the geometry over time. Finally, the development of a suitable resin for volumetric printing has been demonstrated, with hopes of further subsequent resin development in the near future.

Despite the demonstration that this project has delivered, the technology is far from being commercialized into a viable product and thus their are some significant technological advances that need to be achieved to validate this approach. One of the current issues with the approach taken is that the projection software does not have an in-depth understanding of the kinetic effects on the resin. Unlike traditional SLA/DLP printing systems, the curing mechanics are significantly more complex due to the requirement of light to propagate through the polymer without necessarily curing it. Furthermore, this approach takes advantage of oxygen inhibition to enable light propagation without instantaneous solidification, which is usually undesirable in traditional resin based systems. Because of the requirement of oxygen depletion before curing onset, the ability to model and thus predict oxygen depletion rates is also required for accurate reconstruction. Currently the kinetic simulation engine does not consider the effects of oxygen inhibition which in most cases is extremely important in predicting the development of the model. Thus, future versions will need to include this key parameter before being able to completely define the models development.

As observed in many of the printed results, boundaries of the developed geometries tend to lack detail and often appear blurred. This is most likely due to oxygen diffusion into these low dose areas, which in turn leads to spacial blurring. This is an underlying challenge in using resin systems that are susceptible to oxygen inhibition, especially in our case where oxygen is used to prevent instantaneous solidification. One potential solution to this problem is to prevent instantaneous cross-linking through another mechanism that does not rely on oxygen inhibition. One proposed method would be to use photo-inhibition patterning via a secondary projection system. This second projection system would essentially act as a mask to the primary projection, inhibiting polymerization in undesirable locations. Prior artwork has already been shown to work in the two-dimensional case [5] for the application of stereo-lithography, so it is safe to assume that this process could be extended to three dimensions. However, for this process to work significant changes to the photo-polymer will need to take place to include additional polymerization inhibitors that respond to an alternative wavelength

capable of masking the primary light source.

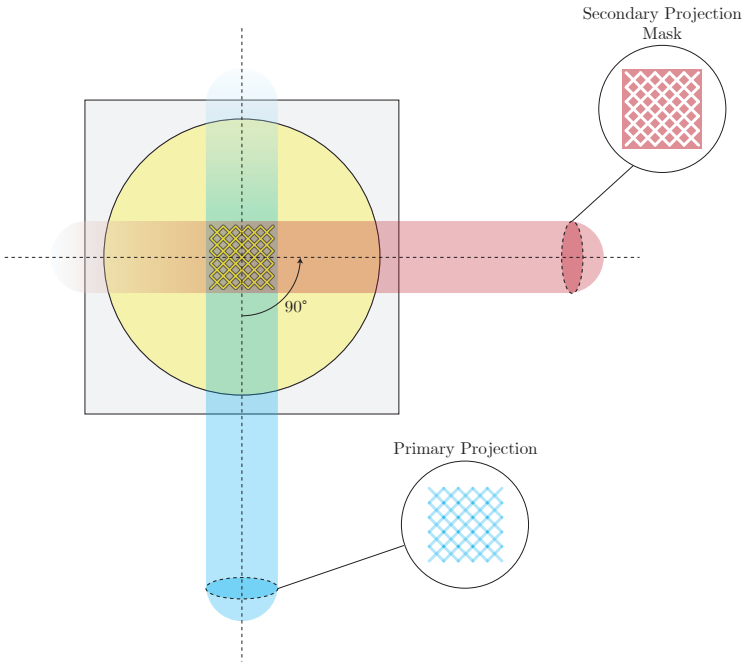

Fig. 5.1 Theoretical basis of design for a printer containing transverse masking of the projection image. This would negate the need for oxygen inhibition by replacing it with a complementary inhibiting wavelength, to reduce the oxygen diffusion mechanism at wall boundaries.

As the concept of this technology is primarily situated upon the already developed literature for computed tomography, many of the reconstruction techniques assume perfect beam propagation. Though tends to be adequate for common imaging methods, for volumetric printing this approach leads to highly inaccurate reconstructions due to the attenuation caused by the pre-polymer and semi-solidified geometry. To account for this, the radon based approach needs to include some correction for beam intensity gradient caused by the absorption of energy by the photo-initiator, in addition to varying attenuation distances caused by the cylindrical geometry. This would enable voxels ahead of the beam to be 'boosted' by subsequent projections to account for intensity non-linearity in the initial projection. Furthermore, it maybe possible to include fan-based tomography approaches to the volumetric printing algorithm, to account for irregularities in image collimation. This addition, albeit significantly more complex to produce a forward model, would enable beam divergence to be included into the projection algorithm, thus negating the requirement for a highly costly optical setup.

It's evident that improving the overall quality of the volumetric approach is not a simple one, as it's dependent on advancements in all aspects of software, hardware and resin development. However, the aspect that is predicted to yield the highest gain is in respect to the mechanical and optical setup used. As the overall size of the print volume increases, the required optical power scales exponentially with the volume. This makes using traditional optical projection systems not viable for large scale production, due to the lack of optical power density. Moving forward it seems logical that laser based approaches tend to produce both a higher power density and improved image clarity compared to their traditional projector counterparts. However, these systems primarily rely on DLP/DMD technology to produce the projection image. This technology, is inherently expensive and has a relatively low damage threshold for higher optical powers which will be required as the volume increases. One potential method to alleviate this constraint is to employ a similar method to traditional strero-lithography where a beam is scanned throughout the volume. This rastering technique could be achieved through the use of an X-Y galvanometer and a collimating lens shown in Fig 5.2.

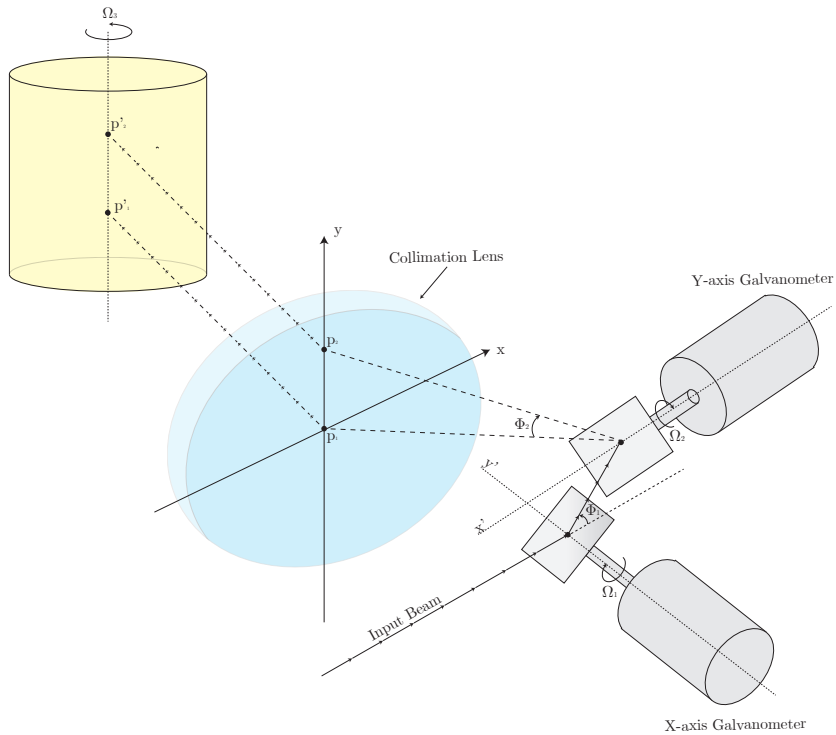

Fig. 5.2 Theoretical design of a new volumetric printing system that incorporates a set of X-Y galvanometers and a high frequency laser pulse to produce a rastered image of the target geometry.

The inherent benefit of this approach, would enable extremely precise and controlled deposition of energy into the volume, which is a significant challenge with projector based systems due to the Gaussian beam distribution of the far-field image. Currently the accuracy of the printer is dominated by the speed at which the volume rotates. Due to attenuation effects caused by the through-thickness curing of the photo-polymer, light tends to be scatted at the behind the object parallel to the projection direction. This can usually be negated by increasing the rotational speed of the volume, to minimize the effect of shadow curing. However, high rotational velocities tends to be unfavorable for print accuracy as instantaneous solidification of the target geometry causes localized mixing and shifting of the topology which reduces the theoretical accuracy of the printer. To alleviate this challenge, it is proposed that a stationary volume with a rotating optical array shown in Fig. 5.3, would yield a significantly better result as the pre-polymer would not be subjected to mixing effects during printing. Thus, in this case the only limiting factor would be the rate in which the volume could be rotated and the update frequency of the projection system which is determined via the refresh-rate of the optical system.

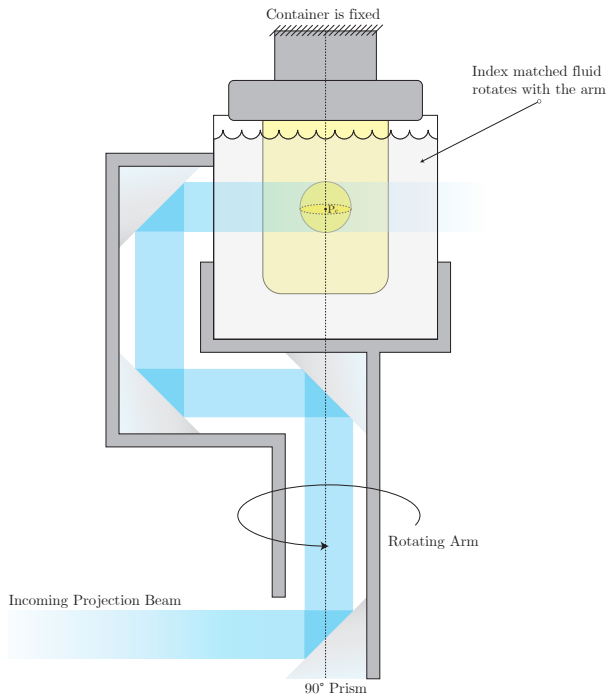

Fig. 5.3 Theoretical design of a new volumetric printing system that incorporates a stationary print volume via the use of a rotating optical array. This will enable the volume to be rotated at a much greater rate without inducing mixing effects within the volume.

Chapter 6

Conclusions

The current work demonstrates a careful design and initial implementation of a new paradigm of additive manufacturing with hope of promoting further development and study into this rapidly emerging field. This project fosters a shift away from the traditional layer by layer approach and toward an obvious holistic approach to the discretization of the target model. This project has demonstrated significant benefits of this method, primarily in regards to surface quality and print speed where volumetric printing is orders of magnitude faster than any currently available process today. The developments highlighted in this work have established a large portion of the proof of concept, specifically in regards to the mechanical system, software package and resin development, enabling a strong foundation in-which to develop further iterations. However, the current design is not without flaws and has significant idiosyncrasies that need to be fleshed-out before this concept can become a reality. However, the hope was that this work has developed a strong basis of theoretical understanding, whist highlighting key recommendations to improve further revisions in the future.

References

[1] Charles Hull. Apparatus for production of three-dimensional objects by stereolithography. *Google Patents*, 1986.

[2] Stephen Y Chou, Peter R Krauss, Preston J Renstrom, Technology B: Microelectronics, Measurement Nanometer Structures Processing, and Phenomena. Nanoimprint lithography. 14(6):4129–4133, 1996.

[3] Paulo Jorge Bartolo. *Stereolithography: materials, processes and applications*. Springer Science and Business Media, 2011.

[4] John R Tumbleston, David Shirvanyants, Nikita Ermoshkin, Rima Janusziewicz, Ashley R Johnson, David Kelly, Kai Chen, Robert Pinschmidt, Jason P Rolland, and Alexander Continuous liquid interface production of 3d objects. 347(6228):1349–1352, 2015.

[5] Martin P de Beer, Harry L van der Laan, Megan A Cole, Riley J Whelan, Mark A Burns, and Timothy F Rapid, continuous additive manufacturing by volumetric polymerization inhibition patterning. 5(1):eaau8723, 2019.

[6] Thierry Rayna, Ludmila Change. From rapid prototyping to home fabrication: How 3d printing is changing business model innovation. 102:214–224, 2016.

[7] S Scott Crump. Apparatus and method for creating three-dimensional objects. *Google Patents*, 1992.

[8] Brett E Kelly, Indrasen Bhattacharya, Hossein Heidari, Maxim Shusteff, Christopher M Spadaccini, and Hayden K Volumetric additive manufacturing via tomographic reconstruction. 363(6431):1075–1079, 2019.

[9] Mukesh Agarwala, David Bourell, Joseph Beaman, Harris Marcus, and Joel Prototyping Journal Barlow. Direct selective laser sintering of metals. 1(1):26–36, 1995.

[10] Carl R Deckard. Method for selective laser sintering with layerwise cross-scanning. *Google Patents*, 1992.

[11] Dinesh K Patel, Amir Hosein Sakhaei, Michael Layani, Biao Zhang, Qi Ge, and Shlomo Highly stretchable and uv curable elastomers for digital light processing based 3d printing. 29(15):1606000, 2017.

[12] Brett E Kelly, Indrasen Bhattacharya, Hossein Heidari, Maxim Shusteff, Christopher M Spadaccini, and Hayden K Volumetric additive manufacturing via tomographic reconstruction. 363(6431):1075–1079, 2019.

[13] Stanley R Deans. *The Radon transform and some of its applications*. Courier Corporation, 2007.

[14] Brett E Kelly, Indrasen Bhattacharya, Hossein Heidari, Maxim Shusteff, Christopher M Spadaccini, and Hayden K Supplementary materials for: Volumetric additive manufacturing via tomographic reconstruction. 363(6431):1075–1079, 2019.

[15] Damien Loterie, Paul Delrot, and Christophe Moser. Volumetric 3d printing of elastomers by tomographic back-projection. 2018.

[16] Paulina Nuñez Bernal, Paul Delrot, Damien Loterie, Yang Li, Jos Malda, Christophe Moser, and Riccardo Volumetric bioprinting of complex living-tissue constructs within seconds. page 1904209, 2019.

[17] R Stephen Davidson. *Exploring the science, technology and applications of UV and EB curing*. Sita Tecnology Limited, 1999.

[18] Christian Decker. Photopolymerization and ultraviolet curing of multifunctional monomers. *Materials science technology*, 2006.

[19] C Decker. Photoinitiated curing of multifunctional monomers. *Acta Polymerica*, 45(5):333–347, 1994.

[20] Bruce M Monroe and Gregory C Weed. Photoinitiators for free-radical-initiated photoimaging systems. *Chemical Reviews*, 93(1):435–448, 1993.

[21] Jean-Pierre Fouassier. *Photoinitiation, photopolymerization, and photocuring: fundamentals and applications*. Hanser, 1995.

[22] Allison O'Brien and Christopher N Bowman. The impact of oxygen on photopolymerization kinetics. 2005.

[23] Shweta Singh, B Rajkumar, Vishesh Gupta, and Akanksha Bhatt. Current photo-initiators in dental materials. 2017.

[24] Yin-Chu Chen, Jack L Ferracane, and Scott A Quantum yield of conversion of the photoinitiator camphorquinone. 23(6):655–664, 2007.

[25] Ewa Andrzejewska, Lars-Åke Lindén, Jan F and Physics. The role of oxygen in camphorquinone-initiated photopolymerization. 199(3):441–449, 1998.

[26] Irini D Sideridou, Maria M Karabela, and Evagelia Ch Vouvoudi. Volumetric dimensional changes of dental light-cured dimethacrylate resins after sorption of water or ethanol. 24(8):1131–1136, 2008.

[27] John W Ceramic stereolithography: additive manufacturing for ceramics by photopolymerization. 46:19–40, 2016.

[28] Jeffrey W Curing dental resins and composites by photopolymerization. 12(6):300–308, 2000.

[29] Shoji Maruo, Osamu Nakamura, and Satoshi Three-dimensional microfabrication with two-photon-absorbed photopolymerization. 22(2):132–134, 1997.

[30] Max S Matheson, EE Auer, Ellen B Bevilacqua, and EJ Chemical Society Hart. Rate constants in free radical polymerization. iii. styrene1. 73(4):1700–1706, 1951.

[31] Steffen Jockusch and Nicholas J Turro. Radical addition rate constants to acrylates and oxygen: alpha-hydroxy and alpha-amino radicals produced by photolysis of photoinitiators. 121(16):3921–3925, 1999.

[32] Shan C Clark, Charles E Hoyle, Sonny Jönsson, Florence Morel, and Christian Decker. Photopolymerization of acrylates using n-aliphaticmaleimides as photoinitiators. 40(18):5063–5072, 1999.

[33] Kristi S Anseth, Cynthia M Wang, and Christopher N Kinetic evidence of reaction diffusion during the polymerization of multi (meth) acrylate monomers. 27(3):650–655, 1994.

[34] Kristi S Anseth, Cynthia M Wang, and Christopher N Reaction behaviour and kinetic constants for photopolymerizations of multi (meth) acrylate monomers. 35(15):3243–3250, 1994.

[35] Kristi S Anseth, Lauren M Kline, Teri A Walker, Karin J Anderson, and Christopher N Reaction kinetics and volume relaxation during polymerizations of multiethylene glycol dimethacrylates. 28(7):2491–2499, 1995.

[36] GR Tryson and AR A calorimetric study of acrylate photopolymerization. 17(12):2059–2075, 1979.

[37] Janina Kabatc, Marek Pietrzak, and Jerzy Cyanine borates revisited. application of the marcus equation for the description of the kinetics of photoinitiated free radical polymerization. iv. 31(14):4651–4654, 1998.

[38] Ewa Andrzejewska, Mariusz B Monomolecular and bimolecular termination in the polymerization of di (meth) acrylates. 198(5):1649–1664, 1997.

[39] Dhananjay Dendukuri, Priyadarshi Panda, Ramin Haghgooie, Ju Min Kim, T Alan Hatton, and Patrick S Modeling of oxygen-inhibited free radical photopolymerization in a pdms microfluidic device. 41(22):8547–8556, 2008.

[40] Teresa G Nunes, L Ceballos, R Osorio, and M Spatially resolved photopolymerization kinetics and oxygen inhibition in dental adhesives. 26(14):1809–1817, 2005.

[41] Johann 1.1 über die bestimmung von funktionen durch ihre integralwerte längs gewisser mannigfaltigkeiten. 5:21, 2005.

[42] Allan Macleod Representation of a function by its line integrals, with some radiological applications. 34(9):2722–2727, 1963.

[43] Godfrey N Computerized transverse axial scanning (tomography): Part 1. description of system. 46(552):1016–1022, 1973.

[44] Gaël Rigaud. *Study of generalized Radon transforms and applications in Compton scattering tomography.* Thesis, 2013.

[45] Joshua D Evans, David G Politte, Bruce R Whiting, Joseph A O'Sullivan, and Jeffrey F Noise-resolution tradeoffs in x-ray ct imaging: A comparison of penalized alternating minimization and filtered backprojection algorithms. 38(3):1444–1458, 2011.

[46] Randolf Hanke, Theobald Fuchs, Norman Methods in Physics Research Section A: Accelerators, Spectrometers, and Associated Equipment. X-ray based methods for non-destructive testing and material characterization. 591(1):14–18, 2008.

[47] Matthias Renker, John W Nance Jr, U Joseph Schoepf, Terrence X O'Brien, Peter L Zwerner, Mathias Meyer, J Matthias Kerl, Ralf W Bauer, Christian Fink, and Thomas J Evaluation of heavily calcified vessels with coronary ct angiography: comparison of iterative and filtered back projection image reconstruction. 260(2):390–399, 2011.

[48] Sarabjeet Singh, Mannudeep K Kalra, Jiang Hsieh, Paul E Licato, Synho Do, Homer H Pien, and Michael A Abdominal ct: comparison of adaptive statistical iterative and filtered back projection reconstruction techniques. 257(2):373–383, 2010.

[49] Tobias Würfl, Mathis Hoffmann, Vincent Christlein, Katharina Breininger, Yixin Huang, Mathias Unberath, and Andreas K medical imaging Maier. Deep learning computed tomography: Learning projection-domain weights from image domain in limited angle problems. 37(6):1454–1463, 2018.

[50] Daniël Pelt, Jan Sijbers, and K Joost Batenburg. Fast tomographic reconstruction from highly limited data using artificial neural networks. pages 109–112, 2013.

[51] Bernhard EH Claus, Yannan Jin, Lars A Gjesteby, Ge Wang, and Bruno De Man. Metal-artifact reduction using deep-learning based sinogram completion: Initial results. pages 631–634, 2017.

[52] F Alberto A study of fourier space methods for "limited angle" image reconstruction. 2(1):31–42, 1980.

[53] Eric Todd Local algorithms in exterior tomography. 199(1):141–148, 2007.

[54] Michel Defrise and Christine De Mol. A regularized iterative algorithm for limited-angle inverse radon transform. 30(4):403–408, 1983.

[55] Gang-rong Qu, Yong-sheng Lan, and English Series Jiang, Ming Mathematicae Applicatae Sinica. An iterative algorithm for angle-limited three-dimensional image reconstruction. 24(1):157–166, 2008.

[56] Yixing Huang, Xiaolin Huang, Oliver Taubmann, Yan Xia, Viktor Haase, Joachim Hornegger, Guenter Lauritsch, Andreas Engineering Express. Restoration of missing data in limited angle tomography based on helgason–ludwig consistency conditions. 3(3):035015, 2017.

[57] Alexandre Goy, Girish Roghoobur, Shuai Li, Kwabena Arthur, Akintunde I Akinwande, and George High-resolution limited-angle phase tomography of dense layered objects using deep neural networks. 2018.

[58] Jawook Gu and Jong Chul Multi-scale wavelet domain residual learning for limited-angle ct reconstruction. 2017.

[59] Chi Zhou, Yong Chen, Zhigang Yang, and Behrokh Khoshnevis. Digital material fabrication using mask-image-projection-based stereolithography. 19(3):153–165, 2013.

[60] Pierre BOHER, Thierry LEROUX, Thibault BIGNON, and Véronique COLLOMB-PATTON. Optical properties of a transparent lcd. 2016.

[61] Alexander Ya Malkin and Avraam I Isayev. *Rheology: concepts, methods, and applications*. Elsevier, 2017.

[62] HP Greenspan and LN On a time-dependent motion of a rotating fluid. 17(3):385–404, 1963.

[63] William B Watkins and RG Spin-up from rest in a cylinder. 20(10):1596–1604, 1977.